

On the Origin and Implications of Li_2O_2 Toroid Formation in Nonaqueous Li-O₂ Batteries

Nagaphani B Aetukuri^{1*}, Bryan D McCloskey^{1,2,3}, Jeannette M. García¹, Leslie E Krupp¹, Venkatasubramanian Viswanathan^{4*} and Alan C. Luntz^{1,5}

1 IBM Almaden Research Center, San Jose, CA, 95120

2 Department of Chemical and Biomolecular Engineering, University of California, Berkeley, CA, 94720

3 Environmental Energy Technologies Division, Lawrence Berkeley National Laboratory, Berkeley, CA, 94720

4 Department of Mechanical Engineering, Carnegie Mellon University, Pittsburgh, PA, 15213

5 SUNCAT, SLAC National Accelerator Laboratory, Menlo Park, CA 94025

**Address correspondence to: phani@alumni.stanford.edu (N.B.A); venkvis@cmu.edu (V.V)*

The lithium-air (Li-O₂) battery has received enormous attention as a possible alternative to current state-of-the-art rechargeable Li-ion batteries given their high theoretical specific energy. However, the maximum discharge capacity in nonaqueous Li-O₂ batteries is limited to a small fraction of its theoretical value due to the insulating nature of lithium peroxide (Li₂O₂), the battery's primary discharge product. In this work, we show that the inclusion of trace amounts of electrolyte additives, such as H₂O, significantly improve the capacity of the Li-O₂ battery. These additives trigger a solution-based growth mechanism due to their solvating properties, thereby circumventing the Li₂O₂ conductivity limitation. Experimental observations and a growth model imply that this solution mechanism is responsible for Li₂O₂ toroid formation. We present a general formalism describing an additive's tendency to trigger the solution process, providing a rational design route for electrolytes that afford larger Li-air battery capacities.

The recent surge in activity seeking batteries with energy densities surpassing that possible with Li-ion intercalation technology is fueled by the goal of developing mass-market electrification of road transportation. The nonaqueous Li-air battery has attracted the most attention to date because of its very high theoretical specific energy¹⁻². In this battery, the net electrochemical reaction is $2 \text{Li} + \text{O}_2 \rightleftharpoons \text{Li}_2\text{O}_2$, with the forward reaction

describing discharge of the battery and the reverse describing charge³⁻⁸. The high theoretical specific energy arises because Li metal is used as the anode and ambient air can act as a source for O₂. At present, there are still substantial technical obstacles to developing a practical Li-air battery⁹⁻¹⁰. Perhaps the most significant challenges arise from parasitic chemistry and electrochemistry during battery cycling¹¹⁻¹⁸ and the electrical passivation of the cathode that occurs during discharge¹⁹⁻²². The first limits rechargeability while the second limits capacity to less than theoretically possible, especially at higher current densities, implying a poor capacity-power tradeoff in the battery²¹. The electrical passivation is caused by the build up of Li₂O₂, a wide band gap insulator during discharge^{3,19-23}. This inhibits charge transfer from the cathode to the Li₂O₂ – electrolyte interface where the discharge electrochemistry occurs.

In ethereal electrolytes, many authors²⁴⁻²⁹ have reported that large Li₂O₂ toroids of variable sizes (100 nm – 1 μm) are produced during discharge at low currents. However, during the course of our studies with nearly anhydrous ethereal electrolytes, we have never observed toroid formation at any current rate, apparently only forming thin conformal coatings of Li₂O₂ on the cathode surface. Understanding the origin of the large toroid features and ultimately controlling the morphology of Li₂O₂ growth during discharge is extremely critical for attaining high discharge capacities since these toroids circumvent the Li₂O₂ charge transport limitations.

In this article, we combine experimental measurements with theoretical modeling to show that there are two possible paths for Li₂O₂ growth on the cathode. One involves a surface electrochemical mechanism previously described^{8,30} that produces conformal Li₂O₂ coatings on the cathode surface whose thicknesses are limited by charge transport through Li₂O₂. We propose that the second path is a solution-mediated electrochemical process driven by LiO₂ partial solubility, where O₂⁻ acts as a redox mediator and ultimately promotes the growth of Li₂O₂ toroids at low currents. Although solution-mediated processes have previously been suggested for the growth of Li₂O₂^{4-5,24,28} neither the electrochemical origins nor the conditions that favor the growth of large toroids have been outlined. In ethereal solvents, we demonstrate that the toroidal growth,

and a concomitant discharge capacity increase, is only observed when trace quantities of H₂O are added to the electrolyte. However, the presence of water also introduces unfavorable consequences for the overall battery electrochemistry. As a result, understanding how H₂O enhances the solubility of LiO₂ allows us to develop insight as to which solvents/additives may induce solution-growth of Li₂O₂ (thereby enhancing the capacity of Li-O₂ batteries), but without the drawbacks that added H₂O introduces.

Figure 1 presents scanning electron microscopy (SEM) images of Vulcan® XC72 carbon cathodes (XC72) extracted from Li-O₂ batteries after galvanostatic discharge to 1 mAh capacity at a current of 50 μA for 500-4000 ppm H₂O added to the electrolyte (1 M Li-TFSI in dimethoxyethane, DME). The Li-O₂ batteries are identical to those used for differential electrochemical mass spectrometry (DEMS) experiments discussed previously¹¹⁻¹² and procedures are described in the methods section of the supplementary information (SI). With no added H₂O, the XC72 cathode after discharge is indistinguishable from the pristine cathode prior to discharge. This suggests that the Li₂O₂ is only deposited as thin conformal films on the cathode surface. However, after addition of 500 ppm H₂O, small thin toroids (100-200 nm in size) become visible in the SEM images. As the H₂O content increases, increasingly larger toroids are formed and layering within the toroids becomes more evident.

Figure 1 clearly shows that the existence of Li₂O₂ toroids in ether-based electrolytes, along with their shape, size and abundance, depends on the concentration of added H₂O in the electrolyte. Previous reports^{24-27,31} indicated toroids with a range of shapes and sizes in ethereal electrolytes and we suggest that this is likely due to varying levels of water contamination in the cells. Figure S1 in the SI shows a diminishment in toroid particle diameter with current at a fixed H₂O content, with no toroids present at currents > 1 mA for 4000 ppm H₂O concentration. At low H₂O content, although toroids are still observed at very low currents, they disappear at currents much lower than 1 mA, in general agreement with prior observations^{24,26,32}. We observe similar discharge morphology changes with increasing H₂O content with other cathodes as well, e.g. TiC and AvCarb® P50 carbon paper (see Figs. S2 and S3 in SI). Toroid morphology is

observed when comparable quantities of water are added to other electrolyte solvents, e.g. tetraethylene glycol dimethyl ether (TEGDME) and dimethylsulfoxide (DMSO) (see Figs. S4 and S5 in SI), thus, suggesting that the presence of H₂O in the electrolyte is the dominant cause of the drastic Li₂O₂ morphology changes.

Additionally, discharge capacity increases as the H₂O concentration increases (Fig. 2a), in agreement with previous studies³³. At low discharge currents (50 μA), this is accompanied with an increase in toroid size. However, even at high currents (3 mA) where no toroid formation is apparent, an increase in discharge capacity is observed with water present (Fig. S10b). We argue that the improvement in capacity at both currents arises due to a solution-mediated mechanism for Li₂O₂ formation (discussed later) that overcomes charge transport limitations inherent in surface growth of Li₂O₂. While trace H₂O has a positive impact on capacity, it is also critical to understand its effect on the battery chemistry and rechargeability.

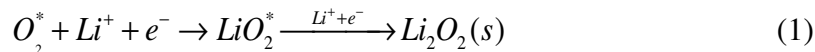
Figure 3a shows X-ray diffractograms (XRD) near the Li₂O₂ (100) and (101) peaks from Avcarb P50 paper cathodes extracted from batteries otherwise similar to those studied in Fig 1. The only additional H₂O-induced XRD feature is a small peak at 30.65 degrees that has tentatively been identified as Li₂NH (Fig. S6). These results confirm that the majority of the crystalline discharge product is Li₂O₂, regardless of electrolyte water content. Notably, no crystalline LiOH is observed in the XRD of the cathodes. The Li₂O₂ diffractograms clearly show a decreasing peak width as a function of increasing water content in the electrolyte solution, implying that the Li₂O₂ crystallite size increases, in agreement with the SEM images shown in Fig 1. Other authors have shown a decrease in XRD linewidth with current (presumably at fixed H₂O content) as the toroid size increases^{24,31,34}. For the nominally anhydrous battery, there was no apparent change in crystallite size with current (see Fig. 3b) Therefore, XRD provides no evidence for a transformation to an amorphous Li₂O₂ deposit at higher currents as suggested by others^{24,35}.

To quantify the effects of added H₂O on the electrochemistry and possible, parasitic reactions, both quantitative DEMS and Li₂O₂ titration were employed¹¹⁻¹². If no parasitic electrochemistry (and chemistry) occurs during discharge, the expected yield of Li₂O₂ produced relative to the theoretical yield from the discharge capacity is unity, $Y_{\text{Li}_2\text{O}_2} = 1.0$. Likewise, two electrons are ideally utilized for each O₂ consumed, $(e^-/\text{O}_2)_{\text{dis}} = 2.00$, where O₂ consumption is monitored using a pressure decay measurement. Figure S7 and S8 in the SI show $(e^-/\text{O}_2)_{\text{dis}}$ and $Y_{\text{Li}_2\text{O}_2}$, respectively. The values without added H₂O are consistent with previous measurements¹² for these low current conditions, i.e. $Y_{\text{Li}_2\text{O}_2} = 0.75$ for an XC72 cathode and $(e^-/\text{O}_2)_{\text{dis}} = 2.02$. However, both deviate further from their optimum values as H₂O is added, demonstrating that the added H₂O induces parasitic processes during discharge. We also note that a titration of both solvent and cathode yields a higher total peroxide content than that from the cathode itself, which we believe is indirect evidence for soluble H₂O₂ formation. It is possible that the additional parasitic chemistry is due to the formation of H₂O₂ and other soluble species, as will be discussed later.

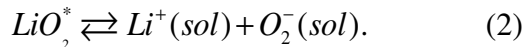
Since H₂O induces parasitic chemistries during discharge, it is not surprising that H₂O impurities also affect the charging potential. Galvanostatic discharge-charge cycles as a function of H₂O content are shown in Fig. S9 in the SI. These profiles demonstrate that although the initial charging potential U_{chg} is nearly identical in all cases, the rate of increase in U_{chg} with charging capacity Q_{chg} is strongly dependent on the H₂O content. We have previously suggested that the initial U_{chg} is indicative of the low Li₂O₂ fundamental kinetic overpotentials³⁰, but that the increase in U_{chg} with Q_{chg} is related to the role of parasitic products in charging³⁶. This interpretation for Fig. S9 in the SI is entirely consistent with the enhanced parasitic chemistry associated with added H₂O (Figs. S7 and S8). Comparing the performance and (electro)chemistry of the anhydrous cells to those with trace amounts of H₂O raises two questions: How does H₂O increase capacity and induce toroid formation? And, is it possible to find another additive that can give the positive benefits of added H₂O without its drawbacks?

Since the dimensions of the toroids are significantly larger than the charge transport-limited dimensions of 1-10 nm, we hypothesize that they must be formed by a solution-mediated mechanism that also contributes to the electrochemistry, as also suggested by others^{24,29}. Thus, the net battery discharge is the sum of the two different contributions. Figure 4a shows discharge linear scan voltammograms (LSV), both with and without added H₂O in DME. The anhydrous DME discharge LSV is similar to that observed previously⁸ and was assigned to the surface process producing Li₂O₂ (the peak at ~2.5 V in Fig. 4a). The discharge LSV curve with 4000 ppm water (Fig. 4b) shows an additional peak at potentials lower than ~2.5 V. We suggest that this additional peak in the LSV is related to the solution-mediated growth of Li₂O₂. This additional peak represents an electrochemical process principally forming Li₂O₂, as indicated by a peroxide titration (Y_{Li₂O₂} = 0.81 following the LSV with 4000 ppm added H₂O in DME). Since current from both surface and solution processes is possible at typical galvanostatic conditions (where a potential plateau ranges from 2.4-2.7 V), both the surface and solution processes can contribute to galvanostatic discharges.

The schematic in Fig. 5 summarizes the two electrochemical paths for Li₂O₂ crystal growth. The surface electrochemical growth is given as before³⁰.



where * refers to a surface adsorbed species and (s) for solid. Both Li⁺ + e⁻ charge transfer or disproportionation ($2LiO_2^* \rightarrow Li_2O_2(s) + O_2$) can contribute to the second step of growth^{8,37}. We also consider a second slower possible route for the growth of Li₂O₂ crystals induced by the generation of soluble reduced oxygen species in the presence of H₂O. The dominant Li₂O₂ equilibrium surface produced by reaction (1) is the O-rich (0001) surface, i.e. a Li₂O₂ surface with half a monolayer of LiO₂ adsorbed^{23,30,38}. Its solubility is given as



The equilibrium is governed by the stability of the Li⁺ and O₂⁻ ions in solution (sol) relative to the LiO₂* adsorption energy on Li₂O₂. As described in detail in the SI, the stability of Li⁺ and O₂⁻ ions in solution is related to the Gutman Donor Number (DN) and

acceptor number (AN), respectively and hence the LiO_2^* solubility depends on these parameters. The addition of water triggers this dissolution process by solvating O_2^- efficiently due to its very high AN of ~55. We believe that the solution soluble O_2^- undergoes subsequent reaction on a growing Li_2O_2 toroid through the generic mechanism

$$2\text{Li}^+(\text{sol}) + 2\text{O}_2^-(\text{sol}) \rightleftharpoons \text{Li}_2\text{O}_2(\text{s}) + \text{O}_2(\text{g}) \quad (3)$$

Many different detailed mechanisms could contribute to reaction (3). However, the key point is that Li_2O_2 solution growth uses $\text{O}_2^-(\text{sol})$ as a redox shuttle. The most likely mechanism (shown in Fig. 5) is that: (a) LiO_2^* solvates in an equilibrium fashion from the O-rich (0001) Li_2O_2 that conformally coats the cathode that was produced via the surface process (1) (since this is the dominant surface area of O-rich (0001) Li_2O_2 formed), (b) $\text{O}_2^-(\text{sol})$ diffuses to a growing particle where it forms LiO_2^* again, (c) two such LiO_2^* disproportionate to form Li_2O_2 on a larger growing particle and (d) LiO_2^* regenerates via reaction (1) at the empty site on the conformal layer. It is worth highlighting that the anhydrous DME has an AN ~ 10 and therefore does not induce enough solubility of LiO_2^* to induce significant solution growth.

In a partially protic solvent (DME with added H_2O), $\text{O}_2^-(\text{sol})$ is known to undergo disproportionation, ultimately forming H_2O_2 . H_2O_2 formation is a relatively slow step in mixed aprotic- H_2O solvents³⁹. However, this step, along with a reaction between H_2O and Li metal, slowly consumes the H_2O and eventually this reduction of water reduces the overall dissolution rate and ultimately terminates the solution growth mechanism.

Based on this mechanism, we developed an electrochemical model that accounts for the simultaneous surface and solution routes to formation of Li_2O_2 , and where appropriate compare with the experiments above. This model also includes the disproportionation of $\text{O}_2^-(\text{sol})$ in the presence of water. The model is described in detail in the SI. The evolution of the different chemical species, H_2O , $\text{O}_2^-(\text{sol})$ and H_2O_2 , during galvanostatic discharges for several different added H_2O contents is given in Fig.

S15. The significant increase in the concentration of $O_2^-(sol)$ in the presence of H_2O promotes the solution mechanism in addition to the surface electrochemical growth of Li_2O_2 and therefore increases the discharge capacity (see Fig. 2b). However, the solution route ultimately shuts off due to a decrease in soluble $O_2^-(sol)$ as the H_2O is consumed by conversion to H_2O_2 and by reaction with the Li anode. This consumption leads to a decreased solubility of $O_2^-(sol)$ which ultimately determines the maximum discharge capacity for a given H_2O content. The maximum discharge capacity, therefore, is a function of the H_2O content in the electrolyte. The results from the model are summarized in Fig 2b and are in qualitative agreement with Fig. 2a, i. e. a ~5 fold enhancement in discharge capacity for the 4000 ppm case relative to the anhydrous case. Using the same model, we also simulate the LSV for 4000 ppm added H_2O in Fig. 4c. This clearly demonstrates the existence of two distinct peaks associated with the surface and solution electrochemical growth routes and is in good agreement with Fig. 4b. Note that the LSV experiments are shifted to lower potentials due to iR losses at these currents²⁰.

Clearly the solution mechanism allows particle sizes (and capacities) larger than the few nm dimensions defined by charge transport. How particles dynamically grow in such a process is a challenging problem. At low currents, large layered toroids are observed. At higher currents (and/or lower H_2O content), much smaller particle sizes are formed. In the SI, we present a plausible kinetic model for the solution growth of these particles. It is based on assuming three coupled kinetic processes; a solution growth rate of Li_2O_2 on the particles, a passivation rate that helps terminate the solution growth (e. g. formation of Li_2NH on the Li_2O_2 particle surface) and a rate for formation of defects/holes in the passivation layer. With reasonable kinetic rates and at low currents, layered toroids are naturally formed via this mechanism, with sizes dependent upon the H_2O concentration and overall current. Two examples are given in Fig 5b and 5c, and an animation of the toroid growth is given in the SI. At higher currents, diffusion limitations of $O_2^-(sol)$ restrict the size of the growing particles, and at lower H_2O concentrations, the shorter times (capacities) available for solution growth restrict the particle size (see Fig.

S1f). An extended discussion of this model and its relationship to the parameters of the solution mechanism are given in the SI.

While added H₂O enhances discharge capacity in ether solvents by inducing a solution mechanism for growth of Li₂O₂, it also induces enhanced parasitic chemistry. A key question is whether other additives/solvents can also induce the solution growth mechanism, but perhaps without the additional parasitic chemistry. As discussed in detail in Section S3, the solubility of LiO₂* is determined by the Gutman DN and AN of the solvent, respectively. Based on experimental measurements on the redox potential shifts for O₂/O₂⁻ and Li/Li⁺, we develop an expression for the relative free energy of dissolution, Eq. (2), on any solvent (see section S3 for details). Fig. 6 shows a contour plot of the free energy of dissolution as a function of AN and DN with several known solvents labeled in the plot. DME and MeCN have limited propensity to solvate LiO₂* and hence are ineffective in promoting solution growth. Of the pure aprotic solvents, DMSO is relatively active because of its high DN. In fact, cathodic LSVs of cells employing DMSO-based electrolytes (see Fig. S12) also exhibit a weak second peak ascribed to the solution-mediated Li₂O₂ formation mechanism. Furthermore, very small toroids are observed on cathodes that are galvanostatically discharged in nearly anhydrous DMSO (~30 ppm water content, see Fig. S5a), at low currents, in agreement with Figure 6, but these grow substantially in size (and layering) with added H₂O. Another possible additive with strong solvating properties is CH₃OH. Addition of 4000 ppm CH₃OH to DME does increase the maximum discharge capacity by ~3x relative to pure DME at 100 μA current (see Fig S10a). The LSV with methanol added to DME (see Fig. S11) also shows an additional peak (although the peak current is smaller compared to H₂O) that we attribute to the solution growth of Li₂O₂. Unfortunately, the pKa of protic CH₃OH is slightly lower than H₂O, so a galvanostatic discharge also produces H₂O₂ and a Y_{Li₂O₂} ~ 0.5 (0.4 mAh discharge capacity).

The enhanced discharge capacity and the growth of large Li₂O₂ toroids in the presence of added water is definitive evidence that the discharge capacity of Li-O₂ batteries need not be limited by the surface growth route and the electronically insulating

nature of Li_2O_2 . The solubility of O_2^- in the battery electrolyte can activate a mechanism where O_2^- acts as a redox mediator for the electrochemical growth of Li_2O_2 that is not limited by the charge transport of Li_2O_2 . The few examples above show that this solution route is not limited to only added H_2O and validates the analysis that lead to the predictions of Fig. 6. Solvents/additives that allow for increased solubility of LiO_2^* will be the key for obtaining large discharge capacities, and we have developed a quantitative basis for the rational selection of solvents based on their acceptor and donor numbers. The desired additive must possess a high DN or/and AN while at the same time possess a high pK_a to avoid H_2O_2 formation and related parasitic processes. The identification of such additives could pave the way towards enhancing the discharge capacity, while still optimizing the rechargeability of the Li- O_2 battery.

AUTHOR CONTRIBUTIONS

All authors contributed to the design of the research. N. B. A., J. M. G., and L. E. K. performed the experimental measurements, and N. B. A. performed the experimental data analysis. V. V. and A. C. L. designed the theoretical calculations, which V. V. then performed. N. B. A., B. D. M., V. V., and A. C. L. co-wrote the manuscript. All authors discussed the results and commented on the manuscript.

Competing financial interests: The authors declare no competing financial interests.

- 1 Imanishi, N., Luntz, A. C. & Bruce, P. G. *The Lithium Air battery*. (Springer New York, 2014).
- 2 Bruce, P. G., Freunberger, S. A., Hardwick, L. J. & Tarascon, J.-M. Li-O₂ and Li-S batteries with high energy storage. *Nature Mater.* **11**, 19-29 (2012).
- 3 Hummelshoj, J. S. *et al.* Elementary oxygen electrode reactions in the aprotic Li-air battery. *J. Chem. Phys.* **132**, 071101 (2010).
- 4 Laoire, C. O., Mukerjee, S., Abraham, K. M., Plichta, E. J. & Hendrickson, M. A. Influence of nonaqueous solvents on the electrochemistry of oxygen in the rechargeable lithium-air battery. *J. Phys. Chem. C* **114**, 9178-9186 (2010).
- 5 Laoire, C. O., Mukerjee, S., Abraham, K. M., Plichta, E. J. & Hendrickson, M. A. Elucidating the mechanism of oxygen reduction for lithium-air battery applications. *J. Phys. Chem. C* **113**, 20127-20134 (2009).
- 6 Abraham, K. M. & Jiang, Z. A polymer electrolyte-based rechargeable lithium/oxygen battery. *J. Electrochem. Soc.* **143**, 1-5 (1996).
- 7 Ogasawara, T., Débart, A., Holzapfel, M., Novák, P. & Bruce, P. G. Rechargeable Li₂O₂ electrode for lithium batteries. *J. Am. Chem. Soc.* **128**, 1390-1393 (2006).
- 8 McCloskey, B. D., Scheffler, R., Speidel, A., Girishkumar, G. & Luntz, A. C. On the mechanism of nonaqueous Li-O₂ electrochemistry on C and its kinetic overpotentials: some implications for Li-air batteries. *J. Phys. Chem. C* **116**, 23897-23905 (2012).
- 9 Girishkumar, G., McCloskey, B., Luntz, A. C., Swanson, S. & Wilcke, W. Lithium-air battery: promise and challenges. *J. Phys. Chem. Lett.* **1**, 2193-2203 (2010).
- 10 Christensen, J. *et al.* A critical review of Li/air batteries. *J. Electrochem. Soc.* **159**, R1-R30 (2011).

- 11 McCloskey, B. D. *et al.* Limitations in rechargeability of Li-O₂ batteries and possible origins. *J. Phys. Chem. Lett.* **3**, 3043-3047 (2012).
- 12 McCloskey, B. D. *et al.* Combining accurate O₂ and Li₂O₂ assays to separate discharge and charge stability limitations in nonaqueous Li-O₂ batteries. *J. Phys. Chem. Lett.* **4**, 2989- 2993 (2013).
- 13 Freunberger, S. A. *et al.* The lithium–oxygen battery with ether-based electrolytes. *Angew. Chem. Int. Ed.* **50**, 8609-8613 (2011).
- 14 Shao, Y. *et al.* Making Li-air batteries rechargeable: material challenges. *Adv. Funct. Mater.* **23**, 987-1004 (2013).
- 15 Assary, R. S., Lau, K. C., Amine, K., Sun, Y.-K. & Curtiss, L. A. Interactions of dimethoxy ethane with Li₂O₂ clusters and likely decomposition mechanisms for Li-O₂ batteries. *J. Phys. Chem. C* **117**, 8041-8049 (2013).
- 16 Younesi, R., Norby, P. & Vegge, T. A new look at the stability of dimethyl sulfoxide and acetonitrile in Li-O₂ batteries. *ECS Electrochem. Lett.* **3**, A15-A18 (2014).
- 17 Bryantsev, V. S. *et al.* The identification of stable solvents for nonaqueous rechargeable Li-air batteries. *J. Electrochem. Soc.* **160**, A160-A171 (2013).
- 18 Bryantsev, V. S. *et al.* Predicting solvent stability in aprotic electrolyte Li–air batteries: nucleophilic substitution by the superoxide anion radical (O₂^{•-}). *J. Phys. Chem. A* **115**, 12399-12409 (2011).
- 19 Albertus, P. *et al.* Identifying capacity limitations in the Li/oxygen battery using experiments and modeling. *J. Electrochem. Soc.* **158**, A343-A351 (2011).
- 20 Viswanathan, V. *et al.* Electrical conductivity in Li₂O₂ and its role in determining capacity limitations in non-aqueous Li-O₂ batteries. *J. Chem. Phys.* **135**, 214704 (2011).

- 21 Luntz, A. C. *et al.* Tunneling and polaron charge transport through Li_2O_2 in Li– O_2 batteries. *J. Phys. Chem. Lett.* **4**, 3494-3499 (2013).
- 22 Radin, M. & Siegel, D. Charge transport in lithium peroxide: relevance for rechargeable metal-air batteries. *Energy Environ. Sci.* **6**, 2370- 2379 (2013).
- 23 Radin, M. D., Feng, T. & Siegel, D. J. Electronic structure of $\text{Li}_2\text{O}_2\{0001\}$ surfaces. *J. Mater. Sci.* **47**, 7564-7570 (2012).
- 24 Adams, B. D. *et al.* Current density dependence of peroxide formation in the Li– O_2 battery and its effect on charge. *Energy Environ. Sci.* **6**, 1772-1778 (2013).
- 25 Fan, W., Cui, Z. & Guo, X. Tracking formation and decomposition of abacus-ball-shaped lithium peroxides in Li– O_2 cells. *J. Phys. Chem. C* **117**, 2623-2627 (2013).
- 26 Mitchell, R. R., Gallant, B. M., Shao-Horn, Y. & Thompson, C. V. Mechanisms of morphological evolution of Li_2O_2 particles during electrochemical growth. *J. Phys. Chem. Lett.* **4**, 1060-1064 (2013).
- 27 Zhai, D. *et al.* Disproportionation in Li– O_2 batteries based on a large surface area carbon cathode. *J. Am. Chem. Soc.* **135**, 15364-15372 (2013).
- 28 Black, R., Adams, B. & Nazar, L. F. Non-aqueous and hybrid Li– O_2 batteries. *Adv. Energy Mater.* **2**, 801-815 (2012).
- 29 Xu, J.-J., Wang, Z.-L., Xu, D., Zhang, L.-L. & Zhang, X.-B. Tailoring deposition and morphology of discharge products towards high-rate and long-life lithium-oxygen batteries. *Nature Commun.* **4** (2013).
- 30 Hummelshoj, J. S., Luntz, A. C. & Nørskov, J. K. Theoretical evidence for low kinetic overpotentials in Li– O_2 electrochemistry. *J. Chem. Phys.* **138**, 034703-034712 (2013).

- 31 Gallant, B. M. *et al.* Influence of Li_2O_2 morphology on oxygen reduction and evolution kinetics in Li- O_2 batteries. *Energy Environ. Sci.* **6**, 2518-2528 (2013).
- 32 Horstmann, B. *et al.* Rate-dependent morphology of Li_2O_2 Growth in Li- O_2 batteries. *J. Phys. Chem. Lett.* **4**, 4217-4222 (2013).
- 33 Meini, S., Piana, M., Tsiouvaras, N., Garsuch, A. & Gasteiger, H. A. The effect of water on the discharge capacity of a non-catalyzed carbon cathode for Li- O_2 batteries. *Electrochem. Solid-State Lett.* **15**, A45-A48 (2012).
- 34 Jung, H.-G. *et al.* A Transmission electron microscopy study of the electrochemical process of lithium-oxygen cells. *Nano Lett.* **12**, 4333-4335 (2012).
- 35 Tian, F., Radin, M. D. & Siegel, D. J. Enhanced charge transport in amorphous Li_2O_2 . *Chem. Mater.* **26**, 2952-2959 (2014).
- 36 McCloskey, B. D. *et al.* Twin problems of interfacial carbonate formation in nonaqueous Li- O_2 batteries. *J. Phys. Chem. Lett.* **3**, 997-1001 (2012).
- 37 Peng, Z. *et al.* Oxygen reactions in a non-aqueous Li^+ electrolyte. *Angew. Chem. Int. Ed.* **50**, 6351-6355 (2011).
- 38 Mo, Y., Ong, S. P. & Ceder, G. First-principles study of the oxygen evolution reaction of lithium peroxide in the lithium-air battery. *Phys. Rev. B* **84**, 205446 (2011).
- 39 Che, Y. *et al.* Water-induced disproportionation of superoxide ion in aprotic solvents. *J. Phys. Chem.* **100**, 20134-20137 (1996).

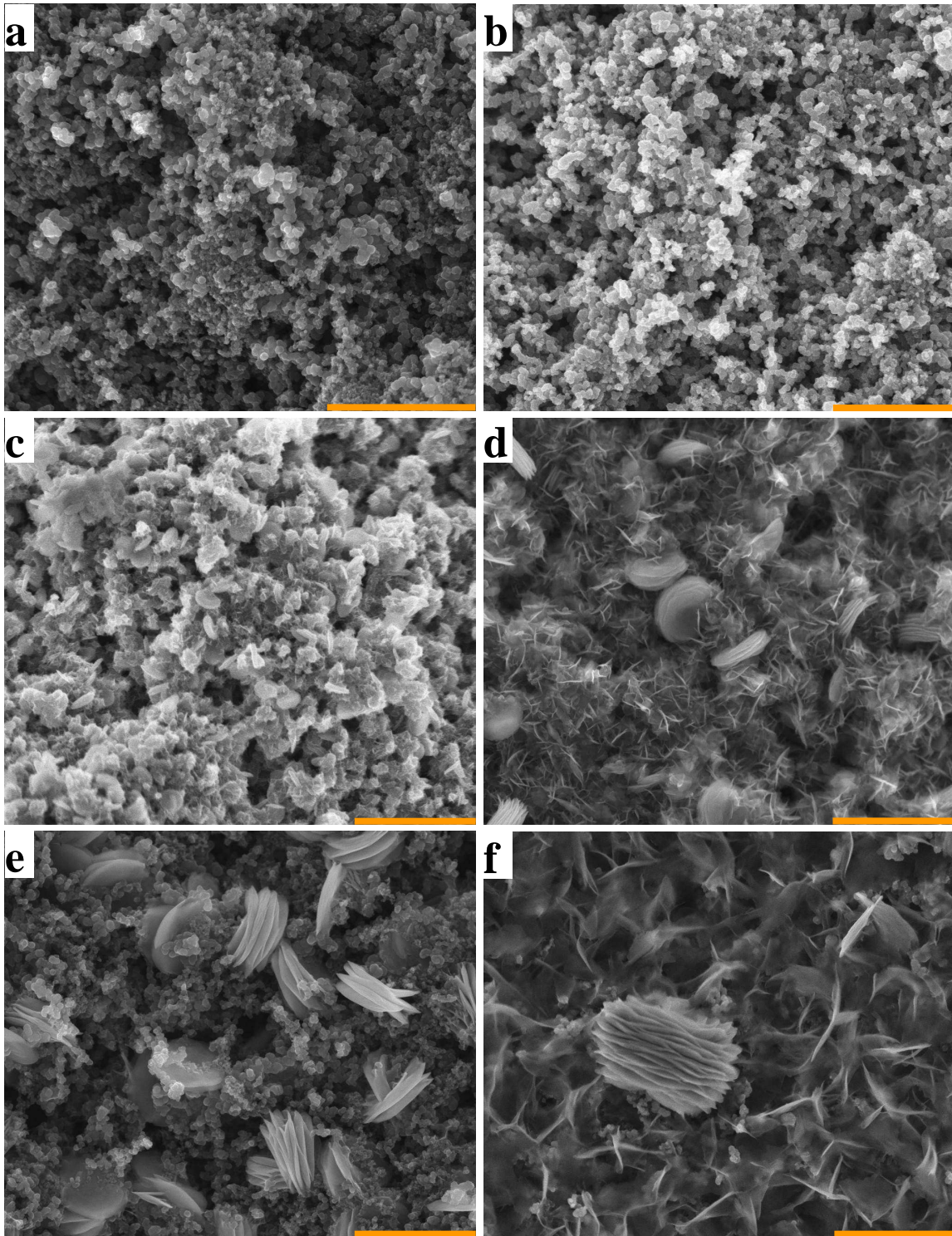


Figure 1, Aetukuri *et. al.*

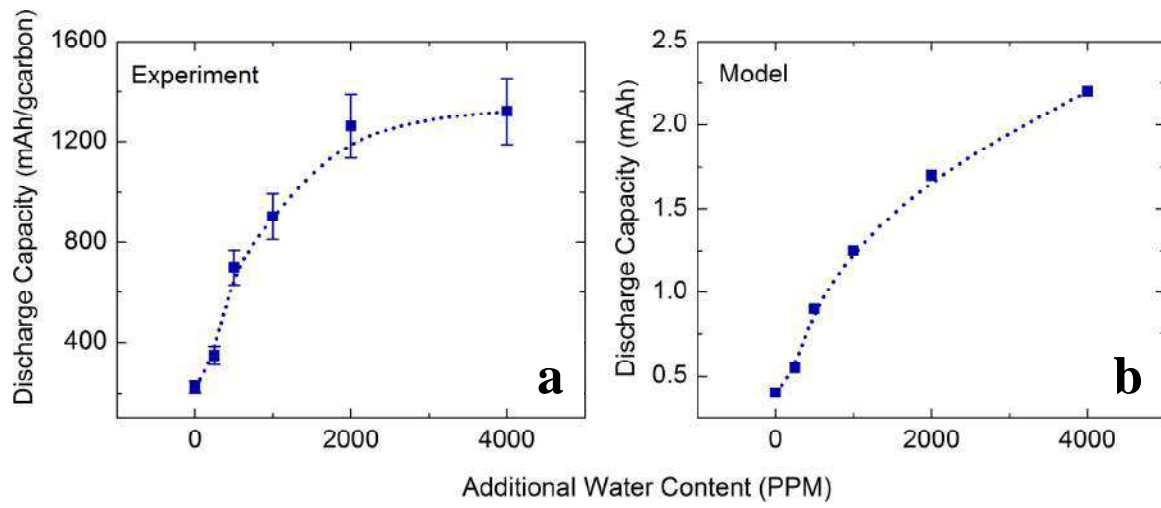


Figure 2, Aetukuri *et. al.*

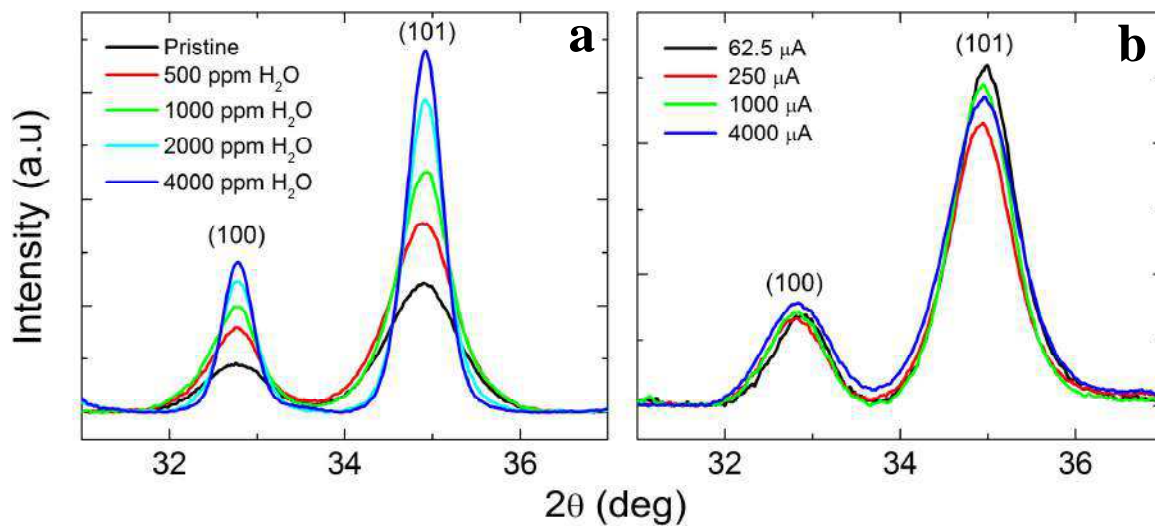


Figure 3, Aetukuri *et. al.*

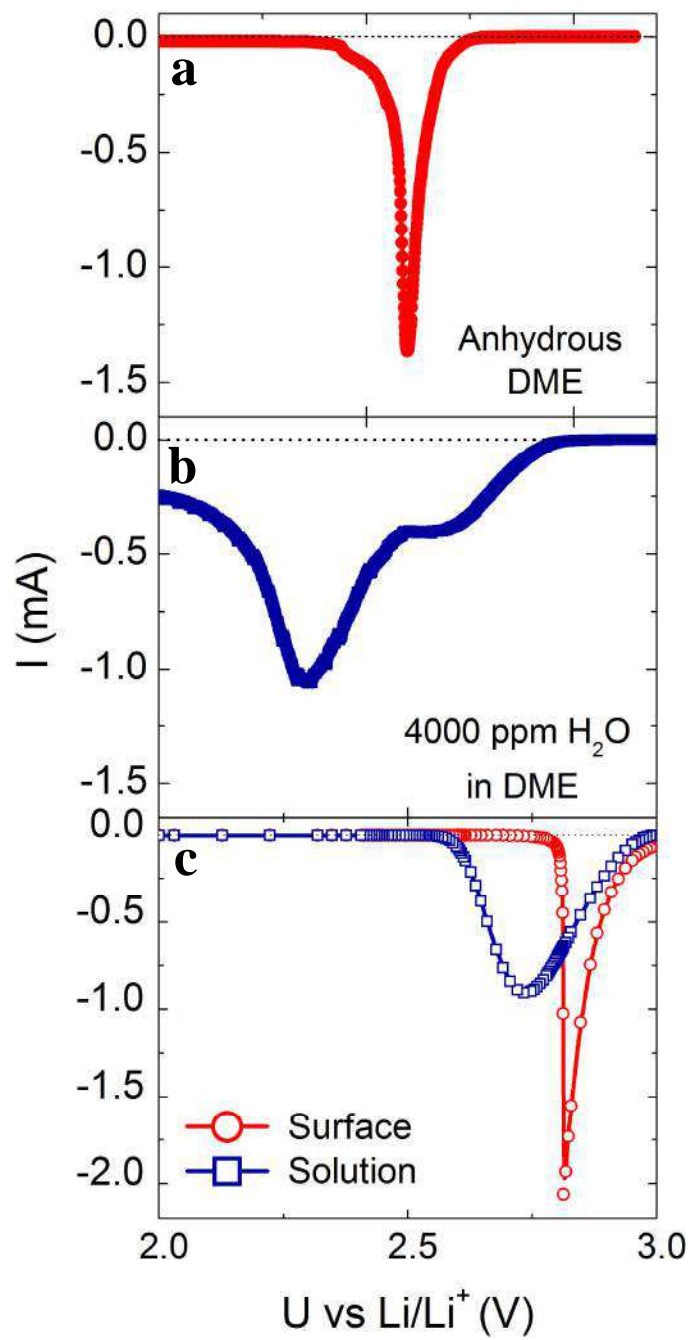


Figure 4, Aetukuri *et. al.*

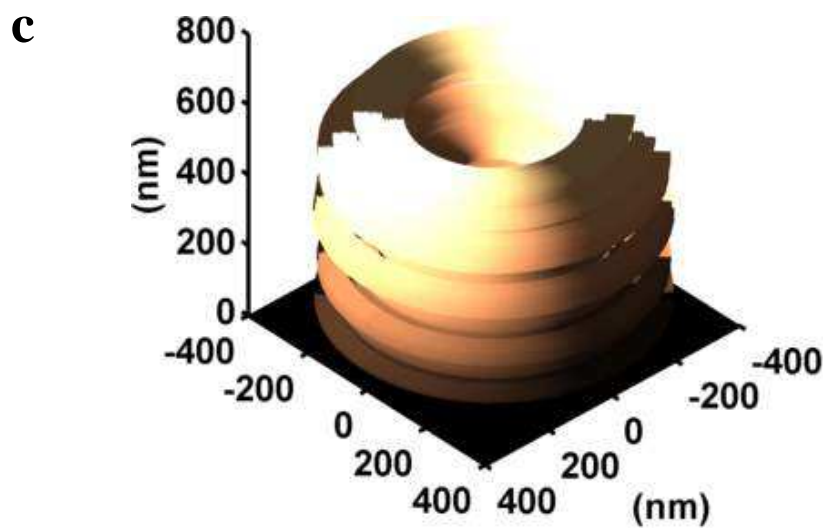
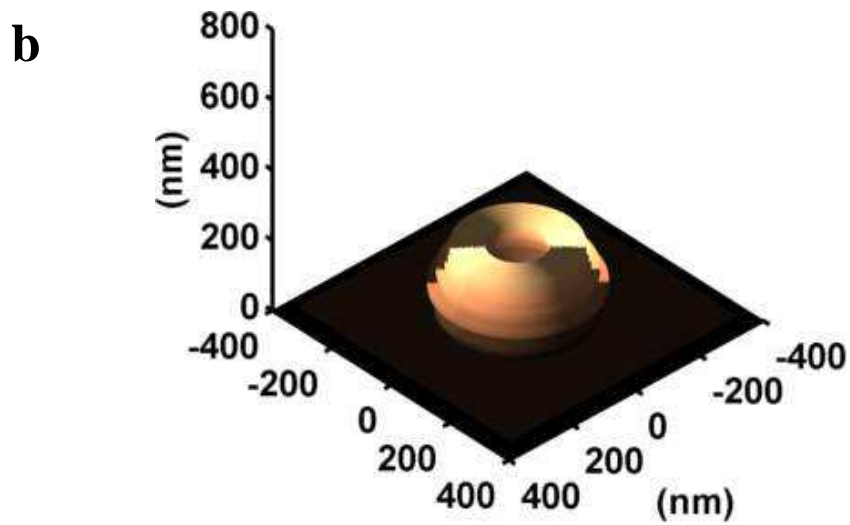
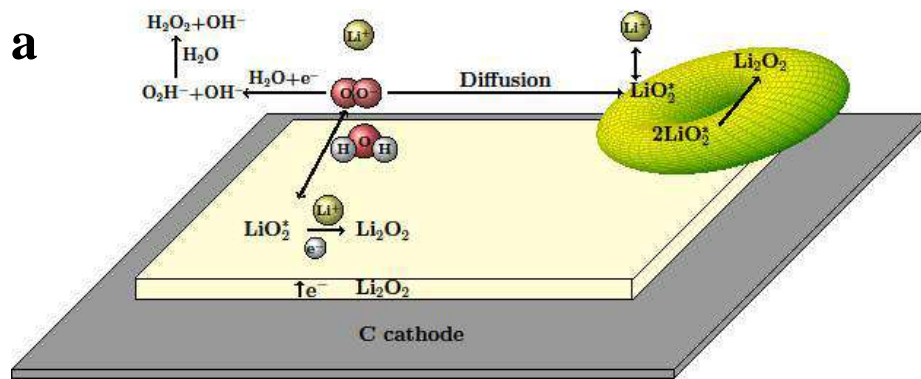


Figure 5, Aetukuri *et. al.*

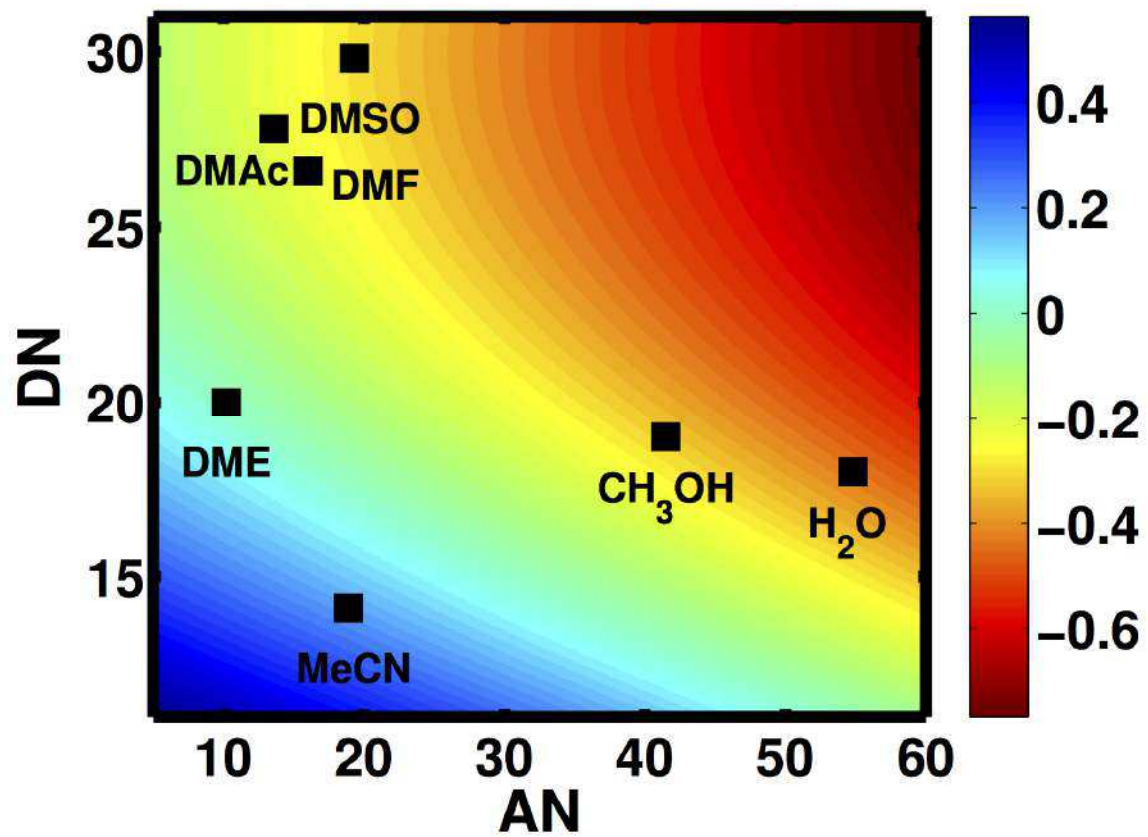


Figure 6, Aetukuri *et. al.*

Figure 1| Li₂O₂ discharge product morphology control. Scanning electron microscopy images of **a**, Vulcan XC72® carbon cathode without any discharge and similar cathodes discharged to a capacity of 1 mAh at a rate of 50 μA using **b**, nominally anhydrous (<30 ppm) 1M Li-TFSI in DME as the electrolyte and **c-f**, with water contents of 500 ppm, 1000 ppm, 2000 ppm, 4000 ppm in the electrolyte. The size of the Li₂O₂ toroids increases with the amount of water in the electrolyte. The thin flake-like features observed in **d** and **f**, we presume increase in size and number of layers to form toroids. All the scale bars are equivalent to 1 μm.

Figure 2| Discharge capacity increase with increasing water content in the electrolyte. **a**, Experimental discharge capacities for batteries employing XC72 carbon cathodes and 1M Li-TFSI in DME with varying water contents as the battery electrolyte. The experimental discharge capacities were obtained from galvanostatic discharges to a reductive potential of 2.3 V (vs Li/Li⁺) at a discharge rate of 200 μA. **b**, Theoretically predicted discharge capacities from the developed electrochemical model. A cathode surface area of ~200 cm² has been assumed for the capacity calculation. The model predicts a ~5 fold enhancement due to the addition of water through the triggering of the solution mechanism. The dotted lines are a guide to the eye.

Figure 3| Ex-situ X-ray diffraction measurements on discharged cathodes. **a**, θ-2θ x-ray diffractograms near the Li₂O₂ (100) and (101) resonance peaks on P50 carbon cathodes discharged at a rate of 250 μA in cells employing 1M Li-TFSI in DME with varying water contents (shown in the legend) as electrolytes. The diffractograms show a strong narrowing of the (100) and (101) peaks with increased water content in the electrolyte which is consistent with increasing Li₂O₂ crystallite size evident from the SEM images of Fig. 1. **b**, Similar diffractograms collected on cathodes discharged at varying discharge rates, as shown in the legend, by employing the nominally anhydrous 1M Li-TFSI in DME electrolyte. No changes in the peak width were observed even by a nearly 2 orders change in the magnitude of the discharge current. This suggests that the Li₂O₂ remains crystalline but the changes in the crystallite size, if any, are below the instrumental resolution in all samples discharged under anhydrous conditions,

irrespective of the discharge rate. All cathodes were discharged to a discharge capacity of 2 mAh and all the curves are normalized to the carbon cathode's (002) x-ray diffraction peak (not shown).

Figure 4| The two pathways for Li_2O_2 formation. Discharge linear scanning voltammograms (LSV) performed at 0.05 mV/s with a Vulcan XC72® carbon cathode and lithium anode employing 1M Li-TFSI based electrolyte solutions in **a**, nominally anhydrous DME **b**, DME with 4000 ppm water. The anhydrous DME sample shows a single sharp peak in the LSV at ~2.5 V. By contrast, the LSV curve for the cell with 4000 ppm water exhibits a distinct second peak at ~2.3 V. We attribute the first peak to surface electrochemical growth of Li_2O_2 and the second peak to the solution-mediated growth of Li_2O_2 where O_2^- acts as a redox mediator. **c**, Theoretically predicted discharge LSV curves for the two independent mechanisms using the developed electrochemical model. The peak currents and the relative potential differences between the two peaks from theory are in good agreement with experiment. The differences in the absolute potentials from theory and experiment could be due to the cell impedance, which is not subtracted from the experimental LSV curves.

Figure 5| Proposed mechanism for the growth of Li_2O_2 toroids in the presence of water. **a**, The deposition of Li_2O_2 in a Li- O_2 cell is shown, schematically, to proceed via a surface electrochemical growth process that occurs on a nucleated film of Li_2O_2 through the sequential transfer of $\text{Li}^+ + e^-$ to the intermediate species, LiO_2^* and eventually forming Li_2O_2 . The electron must, therefore, tunnel through the nucleated Li_2O_2 film as indicated and this process is limited by the electronic conductivity of Li_2O_2 . The presence of a solvent that solvates LiO_2^* to Li^+ and O_2^- (water in our experiments) triggers a solution pathway leading to the growth of toroids, as shown schematically. The soluble O_2^- adsorbs as LiO_2^* on the growing toroidal particle, ultimately disproportionating to form Li_2O_2 . Thus, O_2^- acts as a redox shuttle and leads to the formation of large particles thereby circumventing the conductivity limitations in the surface electro-chemical growth. In our experiments, disproportionation of the O_2^- anion in the presence of H_2O , a proton source, will also lead to the formation of H_2O_2 . However, the dominant

electrochemistry is still the formation of Li_2O_2 (as substantiated in the main text). Li_2O_2 toroidal particle size predicted by the particle growth model developed (and discussed in detail in the SI) for an electrolyte containing **b**, 1000 ppm and **c**, 4000 ppm of water. Larger sized discharge products are observed at higher water contents consistent with the experimental observations.

Figure 6| Quantitative basis for solvent selection for high capacity Li-O₂ batteries.

The free energy of dissolution for LiO_2^* into Li^+ and O_2^- in different solvents as a function of the Gutman acceptor and donor numbers (AN and DN). The free energy plot is normalized relative to that of pure DME. Dimethyl formamide (DMF), dimethyl acetamide (DMAc) and dimethyl sulfoxide (DMSO) have high DN and thus are capable of stabilizing Li^+ . Water and methanol on the other hand, have high acceptor numbers and thus stabilize O_2^- . We predict that solvents that fall in the top right quadrant of this plot will favor solution-mediated deposition of Li_2O_2 , which will be essential for high capacity Li-O₂ batteries.

On the Origin and Implications of Li₂O₂ Toroid Formation in Nonaqueous Li-O₂ Batteries

Nagaphani B Aetukuri^{1*}, Bryan D McCloskey^{1,2,3}, Jeannette G Garcia¹, Leslie E Krupp¹,
Venkatasubramanian Viswanathan^{4*} and Alan Luntz^{1,5}

1 IBM Almaden Research Center, San Jose, CA, 95120

2 Department of Chemical and Biomolecular Engineering, University of California, Berkeley, CA, 94720

3 Environmental Energy Technologies Division, Lawrence Berkeley National Laboratory, Berkeley, CA, 94720

4 Department of Mechanical Engineering, Carnegie Mellon University, Pittsburgh, PA, 15213

5 SUNCAT, SLAC National Accelerator Laboratory, Menlo Park, CA 94025

**Address correspondence to: phani@alumni.stanford.edu (N.B.A); venkvis@cmu.edu (V.V)*

Supplementary Information

S1. Experimental Methods

Cathode Preparation

Vulcan® XC72 (from Cabot Corporation) carbon cathodes were prepared by air spraying a slurry made from 1:3 (m/m) 60 wt% PTFE emulsion and XC72 filtered through a 60 mesh sieve in 20:80 (v/v) isopropanol and water mixture onto a stainless steel mesh. Prior to spraying, the stainless steel mesh is cleaned in running water, isopropanol and then acetone and dried at 130 °C under ambient atmosphere. The carbon coated mesh is air dried at room temperature (RT). TiC cathodes were prepared by plastering a slurry comprising of 1:5 (m/m) 60 wt% PTFE emulsion and TiC nanopowder (SkySpring Nanomaterials, ~40 nm) in isopropanol onto a similarly cleaned stainless steel mesh as done for XC72 carbon cathodes. After plastering TiC, the mesh is air dried at RT. 12 mm diameter carbon cathodes were punched out from the air dried stainless steel meshes in the case of XC72 and TiC or from AvCarb® P50 sheet (from the Fuel Cell Store) for P50 cathodes. The punched cathodes are placed in separate glass vials and further rinsed twice in IPA, dried in vacuum at 130 °C for at least 12 hours and

transferred to an Ar filled glove box with <0.1 ppm water at all times. In the glove box, the cathodes are rinsed twice in DME and dried at 180 °C for at least another 12 hours before using them in Li-O₂ cells. The final carbon loading on the stainless steel mesh is 1.5 – 2 mg.

Electrolytes

Lithium bis(trifluoromethane sulfonyl)imide (Li-TFSI) was the preferred lithium salt for all the experiments reported in this manuscript. 1M Li-TFSI in 1,2 dimethoxy ethane (DME) electrolyte, Li-TFSI salt and the solvents tetraethylene glycol dimethylether (TEGDME) and Dimethyl Sulfoxide (DMSO) were purchased from Novolyte® technologies (now BASF corporation). The water content in all nominally anhydrous electrolytes, measured by Karl-Fischer titration, is <30 ppm. Ultrapure de-ionized (DI) water (18.2 MΩ-cm, Millipore) was used for preparing electrolytes with known quantities of water.

Electrochemical Measurements

All electrochemical measurements were carried out at room temperature on an in-house designed differential electrochemical mass spectrometry (DEMS) system described in detail previously¹⁻². A VMP3 BioLogic multi-channel potentiostat was used for all electrochemical characterization. The DEMS' unique design allows either pressure decay/rise measurements or mass spectrometry to be used to quantify gas consumption and evolution from battery cells. Hermetic electrochemical cells, based loosely on a Swagelok®-type battery cell, are designed to seal by compressing o-rings against a quartz-tube that houses all cell contents. Cells are assembled in an argon glove box with <0.1 ppm water. 11 mm diameter lithium discs punched from an as received 250 μm thick lithium foil (Lectro® Max100 from FMC) were used as anodes for all the cells in this study. Whatman® QM-A grade quartz filters were used as porous electrode-separators when DMSO-based electrolytes were employed and Celgard® 2500 separators were used at all other times. 75 μl of the electrolyte is used when the QM-A separator is used and 65 μl of the electrolyte when the Celgard® separator is used. A 1 mm in height stainless steel ring is used to incorporate a headspace above the cathode. Capillaries

soldered into the cathode side of the cell allow gases to be swept through the cell. All discharges (reduction) were done under constant volume conditions in pure oxygen (research purity grade oxygen from Matheson Tri-Gas®) with a starting pressure of ~1200 Torr. Pressure decay was monitored during discharge to calculate oxygen consumption. Battery charge was carried out in ~950 Torr Argon (research purity grade from Matheson Tri-Gas®) under constant pressure conditions after flushing out any residual oxygen in the cell. All gases (Ar and O₂) were passed through Pur-Gas in-line moisture traps (gas purity >6.0, Matheson Tri-Gas®) prior to being fed to the DEMS, and only copper or stainless steel tubing was used to feed gases to the cell. In between measurements, all gas lines in the DEMS were kept under vacuum and the system was used only if out-gassing under vacuum was not observed (as monitored using the in-line pressure transducers). All connections in the feed lines, DEMS, and a cell assembled without any battery components were He leak-checked under vacuum to ensure complete hermetic integrity.

Chemical Titrations

The chemical titrations performed for these studies are based on the protocol developed by McCloskey *et al*¹⁻². We only give a brief description of the procedure here. All titrations were performed on XC72 cathodes discharged in DME-based electrolytes with varying water contents as noted in the main text. Within 5 min after a discharge, the cathodes were extracted from the cells in an argon glove box (<0.1 ppm water), transferred into a glass vial and placed in a vacuum chamber, connected to the glove box, for 30 min to evaporate volatile constituents including DME, the electrolyte solvent. Next, the glass vial is sealed with a silicone septa lid and transferred out of the glove box. ~2 mL of ultrapure DI water (18.2 MΩ-cm, Millipore) is then injected into the sealed vial using a syringe. The vial contents are stirred for ~30 seconds to improve the reaction rate of the discharge products with water. The base formed by the reaction of the discharge products with water is titrated using standardized 0.005M HCl solution and phenolphthalein as the end-point indicator.

Hydrogen peroxide (H_2O_2) formed by the reaction of Li_2O_2 formed during discharge with the water added to the vial is determined by an iodometric titration. For this titration, 1 mL of 2 wt% KI in H_2O , 1 mL of 3.5 M H_2SO_4 and 50 μL of a molybdate-based catalyst are added to convert the analyte, H_2O_2 , to I_2 . This turns the solution to a pale yellow color. The I_2 thus formed is immediately titrated with 0.01N NaS_2O_3 until the solution turns a faint straw color. ~ 0.5 mL of 1% starch solution is now added for precise end-point detection. The solution turns dark blue after the addition of starch and the titration is resumed and continued until it turns clear. A Metrohm Dosino 800 automatic dispenser was used for the peroxide titration, a Hirschman Solarus burette was used for the acid-base titration. All chemicals used for titrations are purchased from Sigma-Aldrich®.

X-ray Diffraction Measurements

All X-ray measurements were performed on P50 cathodes discharged in DME-based electrolytes. P50 was chosen for x-ray measurements as these cathodes allowed us to discharge the cells to higher capacities (ca. 2 mAh) which is essential for high signal to noise ratio. Cells discharged to 2 mAh were transferred to an argon glove box (<0.1 ppm water) and the cathodes were extracted and placed in a glass vial. The cathodes were twice rinsed in DME to wash off the electrolyte salt and the residual solvent was evaporated in a vacuum chamber, connected to the glove box, for ~ 5 min. The glass vials are moved back to the glove box from the vacuum chamber and the dried cathodes are placed in a custom-built x-ray cell which is o-ring sealed with a kapton® polyimide film. The assembled x-ray cell with the discharged cathode is used for x-ray measurements.

X-ray diffraction (XRD) measurements were performed on a Bruker D8 Discover X-ray diffractometer fitted with a 2-dimensional (2D) X-ray detector. All scans were performed with the detector and incident beam in a symmetric θ - 2θ geometry using graphite monochromated Cu- $K\alpha$ X-rays ($\lambda = 1.5418 \text{ \AA}$) collimated in a pin-hole collimator to yield $\sim 650 \mu\text{m}$ diameter X-ray beam on the sample being measured. Data is collected at room temperature in the 2D mode with an integration time of at least 30 minutes for each frame. During measurements, the discharged cathode is oscillated in the

x-y plane (the sample plane) with 2 mm oscillation amplitude. Therefore, the X-ray diffractograms represent a spatial average over an area of at least 4 X 4 mm² on the cathode. The collected data (at least four frames to cover a 2 θ range of 80 degrees) is integrated over χ , the polar angle orthogonal to 2 θ to yield the intensity vs 2 θ plots shown in the manuscript. We did not find any noticeable changes in the XRD patterns over the measurement time.

Scanning Electron Microscopy

Discharged cathodes used for scanning electron microscopy (SEM) measurements are treated similarly to the cathodes used for x-ray measurements. The dried cathodes are mounted on an SEM sample holder and taken to the SEM sample loading chamber (connected to the SEM) in a sealed glass bottle. The sample holder is then transferred to the sample loading chamber and the latter is then pumped out before transferring the sample holder for imaging in the SEM. The time from opening the glass bottle to the commencement of loading chamber pump down is < 5 seconds. While this procedure prohibits us from performing any quantitative chemical analysis in the SEM, we assume that the change in morphology of the Li₂O₂ particles is negligible for such a short time exposure to ambient. The measurements were performed on an FEI Helios Nanolab 400s system. Imaging was done at an electron current of 43 pA and an accelerating voltage of either 3 or 5 kV. The images presented in this manuscript were collected with a through-lens detector.

S2. Supplementary Text and Figures: Experiment

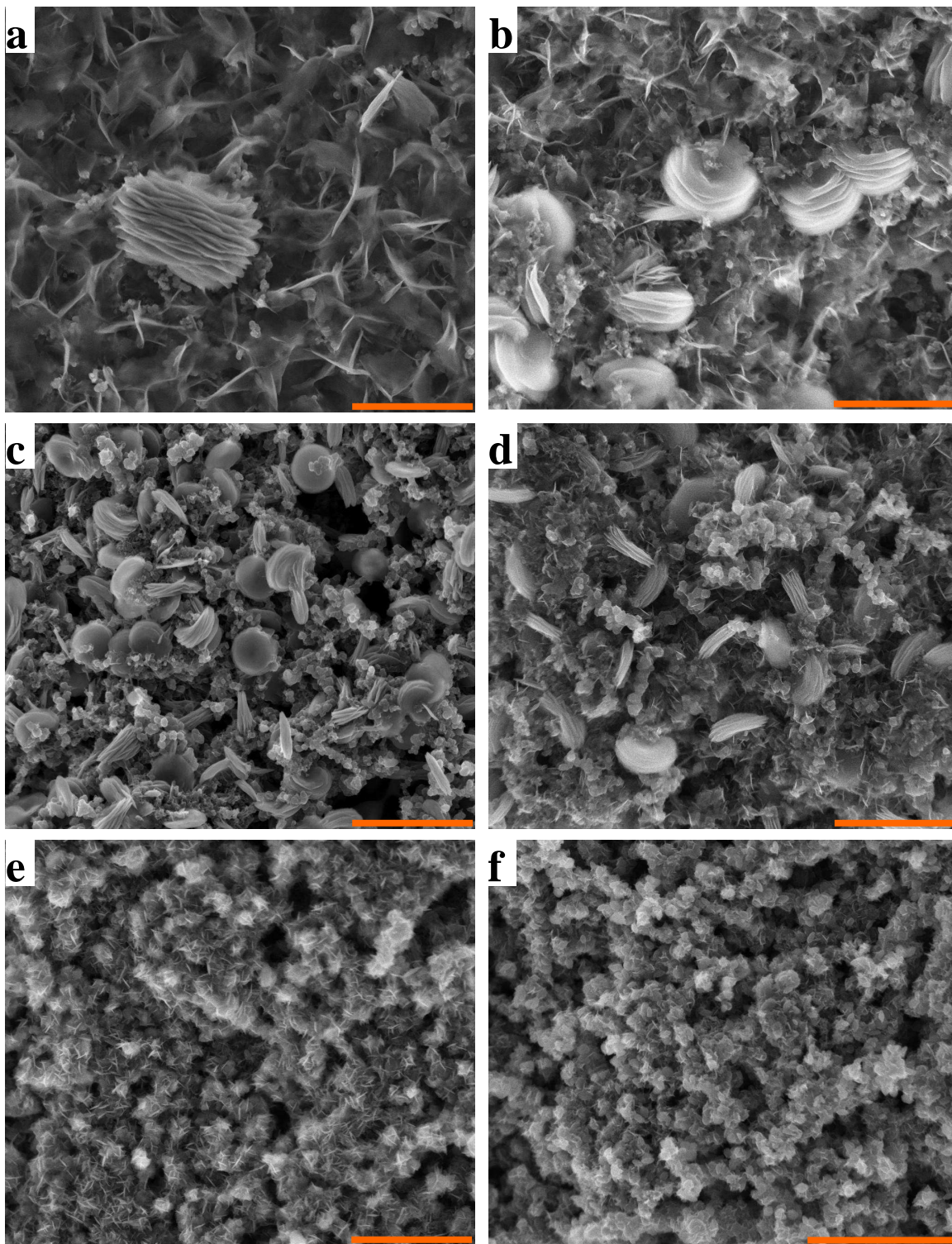


Figure S1| Li_2O_2 toroid size as a function of discharge current. SEM images collected on discharged XC72 cathodes from cells employing 1M Li-TFSI in DME with 4000 ppm

water as an electrolyte and discharged to a capacity of 1 mAh at a discharge rate of **a**, 50 μA **b**, 100 μA **c**, 200 μA **d**, 400 μA **e**, 800 μA and **f**, 1600 μA . All scale bars are equivalent to 1 μm . Clearly, the toroid size is strongly correlated with the discharge rate.

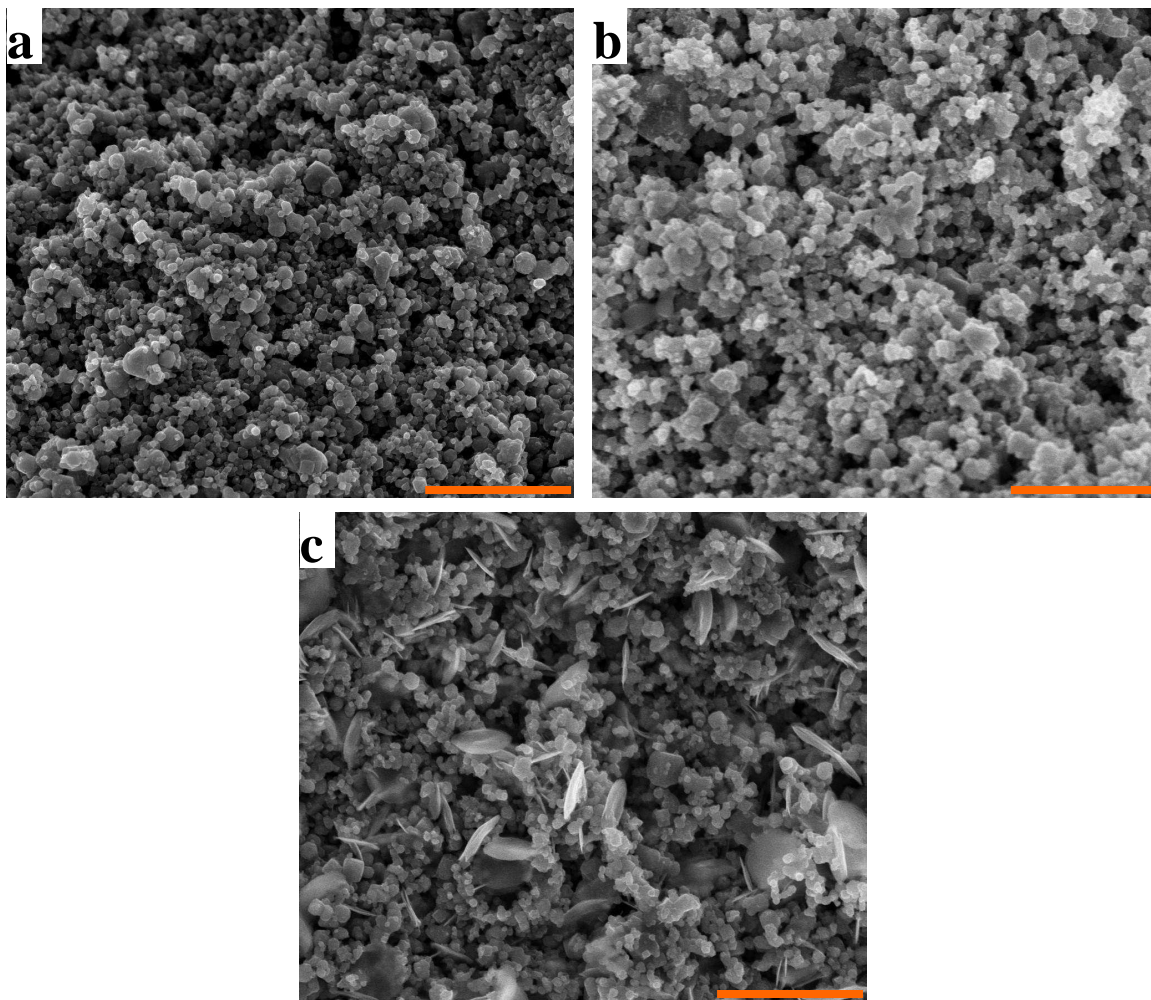


Figure S2| Li_2O_2 morphology control on TiC cathodes. SEM images of **a**, TiC cathode without any discharge and similar cathodes discharged at a rate of 200 μA using **b**, nominally anhydrous (<30 ppm) 1M Li-TFSI in DME as the electrolyte and **c**, with a water content of 4000 ppm in the electrolyte. The size of the Li_2O_2 toroids directly correlates with the amount of water in the electrolyte showing that the morphology changes are not restricted to a particular cathode material. The cathode in **b**, is discharged to a capacity of 0.83 mAh (full discharge capacity at 200 μA) and in **c**, to 1mAh. All the scale bars are equivalent to 1 μm .

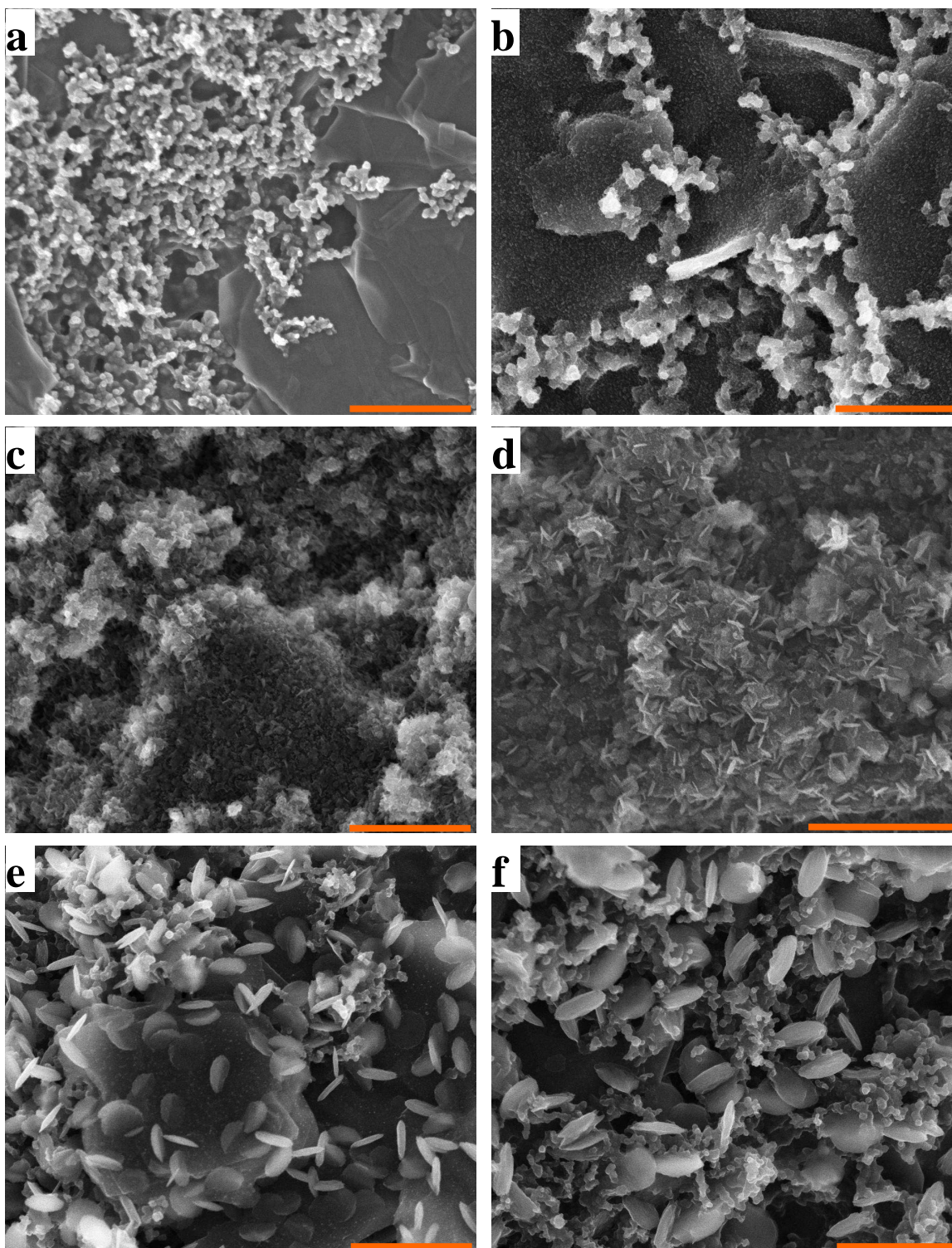


Figure S3| Li_2O_2 morphology control on P50 cathodes. Scanning electron microscopy images of **a**, P50 carbon cathode without any discharge and similar cathodes discharged to a capacity of 2 mAh at a rate of 250 μA using **b**, nominally anhydrous (<30 ppm) 1M

Li-TFSI in DME as the electrolyte and **c-f**, with water contents of 500 ppm, 1000 ppm, 2000 ppm, 4000 ppm in the electrolyte. This toroid-size – water-content correlation observed here is entirely consistent with that presented on XC72 carbon cathodes in the main text (Fig. 1). The SEM imaging on these cathodes was performed after XRD measurements (presented in Fig. 3a of main text) were performed. All the scale bars are equivalent to 1 μm . SEM imaging on the electrode separators (Celgard and QM-A) did not show any toroids even with the highest water content in the electrolyte.

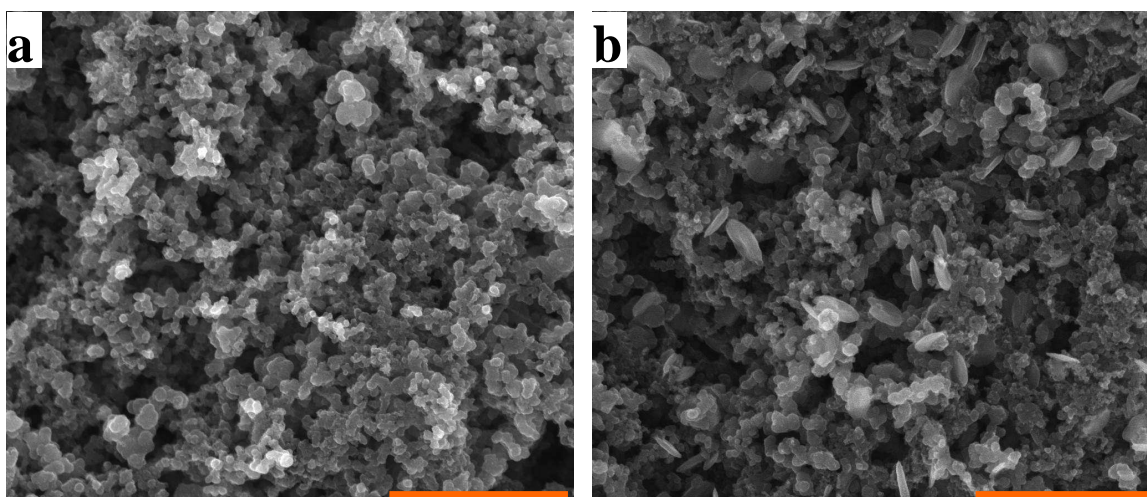


Figure S4| Li_2O_2 morphology control with TEGDME as the electrolyte solvent. SEM images of XC72 cathodes discharged at a rate of 200 μA using **a**, nominally anhydrous (<30 ppm) 1M Li-TFSI in TEGDME as the electrolyte and **b**, with a water content of 4000 ppm in the electrolyte. The size of the Li_2O_2 toroids directly correlates with the amount of water in the electrolyte showing that the morphology changes are similar to those observed with DME. The cathode in **a** is discharged to a capacity of 0.46 mAh (full discharge capacity at 200 μA) and in **b** to 1mAh. All the scale bars are equivalent to 1 μm .

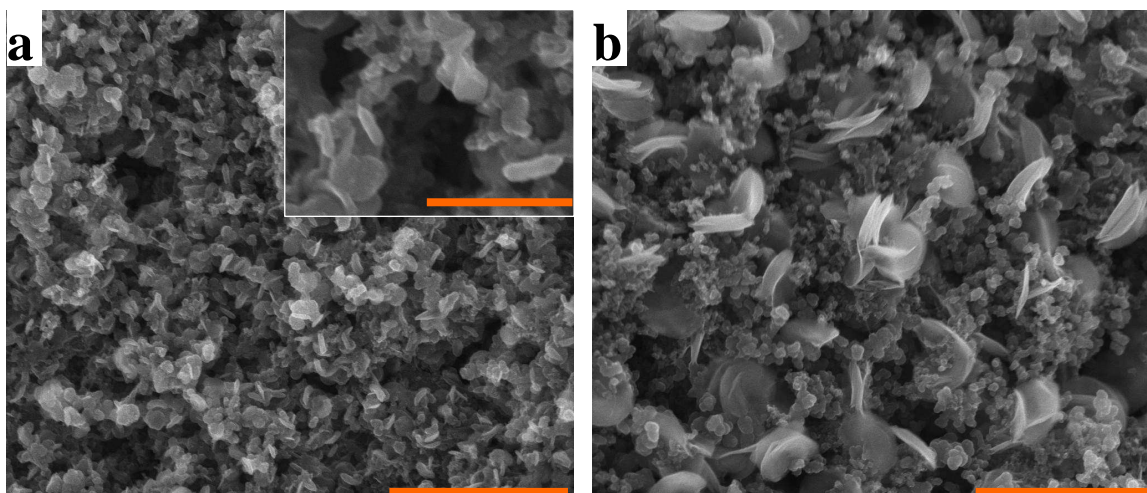


Figure S5| Li_2O_2 morphology control with DMSO as the electrolyte solvent. SEM images of XC72 cathodes discharged at a rate of $200\ \mu\text{A}$ to a capacity of 1 mAh using **a**, nominally anhydrous ($<30\ \text{ppm}$) 1M Li-TFSI in DMSO as the electrolyte and **b**, with a water content of 4000 ppm in the electrolyte. The size of the Li_2O_2 toroids directly correlates with the amount of water in the electrolyte showing that the morphology changes are similar to those observed with DME. However, in the case of DMSO very small toroids, few tens of nanometers in diameter, can be seen (see inset in **a**) even in the nominally anhydrous case. The scale bars in **a** and **b** are equivalent to $1\ \mu\text{m}$. The scale bar for the inset in **a** is equivalent to 300 nm.

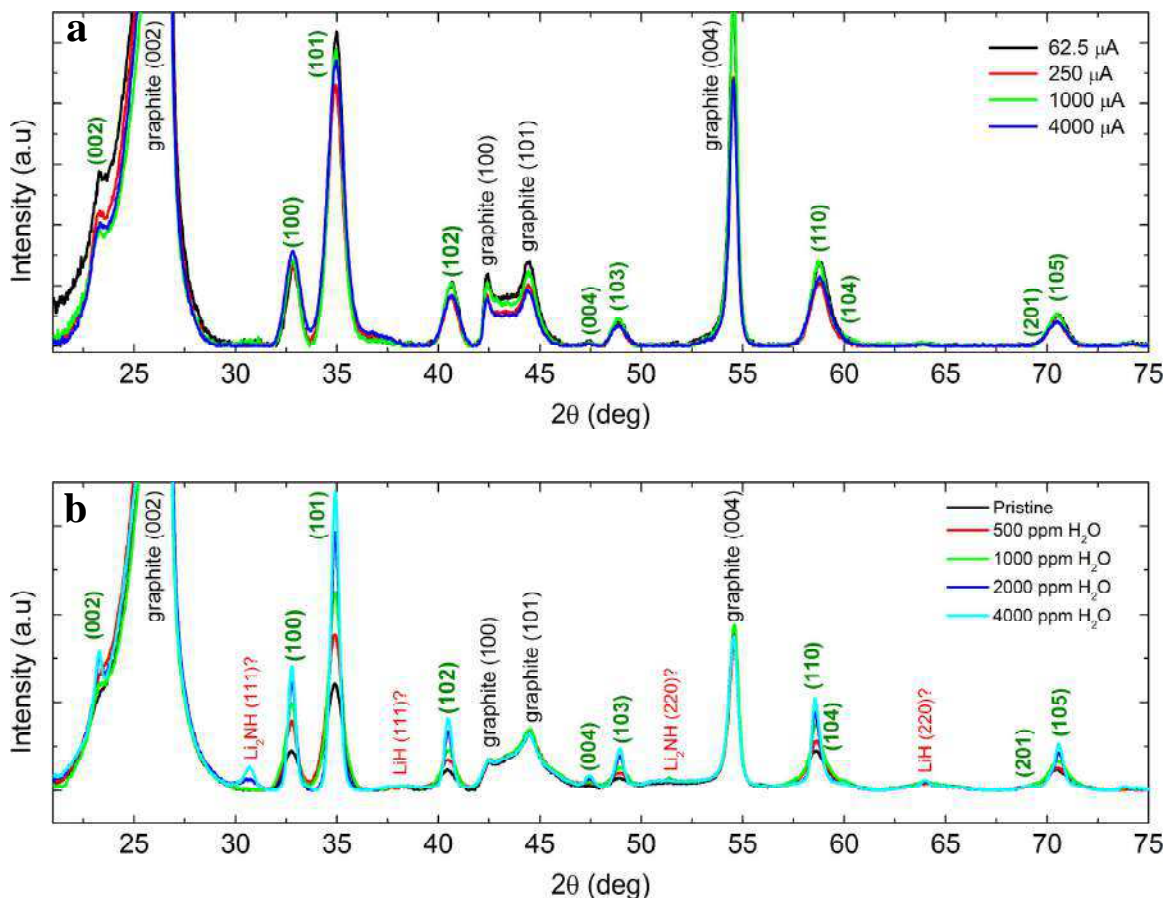


Figure S6| Discharge rate and water-content dependent crystallinity changes. a, Wide angle x-ray diffraction θ - 2θ plot for cells employing the nominally anhydrous electrolyte (1M Li-TFSI in DME) and discharged at currents from $62.5 \mu\text{A}$ to $4000 \mu\text{A}$, as shown in the legend. All peaks can be indexed³ to Li_2O_2 (labels in green color font) and graphite (from the P50 carbon cathode). **b,** Similar XRD θ - 2θ plot for cells discharged at $250 \mu\text{A}$ with the nominally anhydrous electrolyte and electrolytes with added water from 500 ppm - 4000 ppm, as shown in the legend. In addition to the peaks that can be indexed⁴⁻⁵ to Li_2O_2 (labels in green color font) and graphite, an impurity peak at ~ 30.65 degrees can be tentatively attributed to be the Li_2NH (111) peak⁴⁻⁵. Other possible impurity peaks are also indexed in this diffractogram. All cells were galvanostatically discharged to a discharge capacity of 2 mAh. The slight difference in the graphite (100) and (101) peaks in **a** and **b** are presumably because the P50 carbon cathodes are from two different batches.

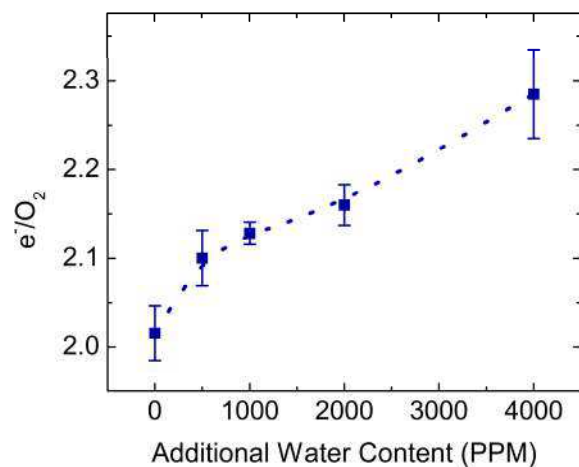


Figure S7| Discharge electrochemistry in electrolytes with water additive. A plot of the number of electrons consumed per oxygen molecule, obtained from pressure decay measurements during cell discharge in pure oxygen, as a function of water content in the 1M Li-TFSI in DME electrolyte. The e^-/O_2 values are an average over at least five different cells for each water concentration and the error bars represent the standard deviation. The electrochemical formation of Li_2O_2 involves two electrons per oxygen molecule. The deviation from this ideal number with increasing water content is indicative of parasitic electrochemistry that is occurring in the cell at high water contents. The dashed line is a guide to the eye.

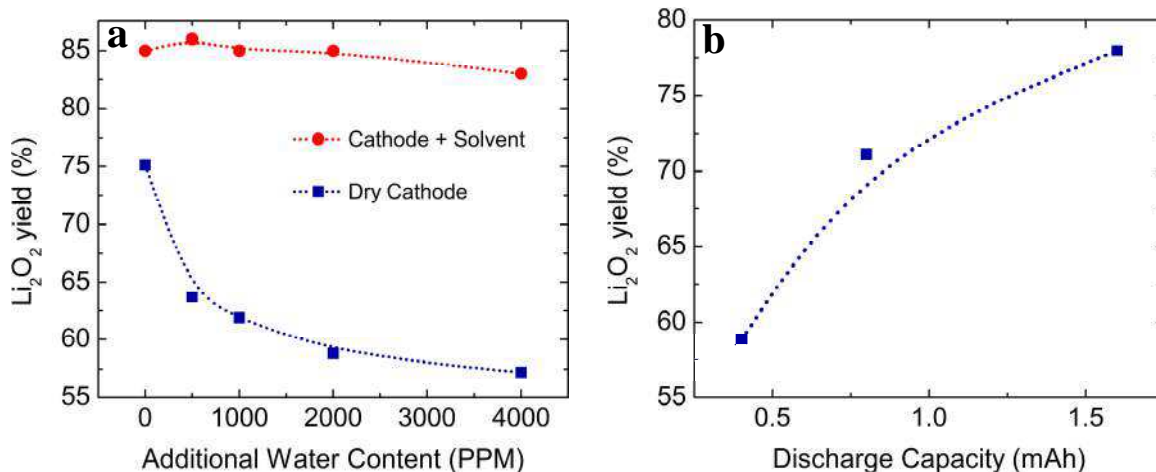


Figure S8| Summary of chemical titrations. a, A plot of the Li_2O_2 yields obtained from iodometric titration experiments performed on XC72 cathodes discharged to a capacity of $400 \mu\text{Ah}$ at a discharge rate of $100 \mu\text{A}$ Li_2O_2 by employing 1M Li-TFSI in DME based electrolytes with varying water contents as shown on x-axis. The cathodes were dried in vacuum for 30 min (see methods section for details). Li_2O_2 yield is defined as the percentage of the titrated peroxide quantity to the expected quantity of Li_2O_2 based on the discharge capacity. Also, included are the titrations performed on the cathodes with most of the electrolyte solvent not evaporated. We take the difference in the titrated peroxide quantities under dry and wet (cathode+solvent) conditions as an indirect measurement for the amount of H_2O_2 generated by the disproportionation of O_2^- in the presence of water. **b,** The titrated Li_2O_2 quantity as a function of discharge capacity for cells employing 1M Li-TFSI in DME with 2000 ppm added water as an electrolyte. This data suggests that most of the capacity enhancement in the batteries with added water is due to the formation of Li_2O_2 . Note that the Li_2O_2 yield is a function of the discharge rate even for the anhydrous sample. For example, samples discharged to $400 \mu\text{Ah}$ at a discharge rate of $100 \mu\text{A}$ and $500 \mu\text{A}$ showed $Y_{\text{Li}_2\text{O}_2}$ values of 75% and 82% respectively. This is consistent with our previously published results⁶. The dotted lines in the both the plots are a guide to the eye.

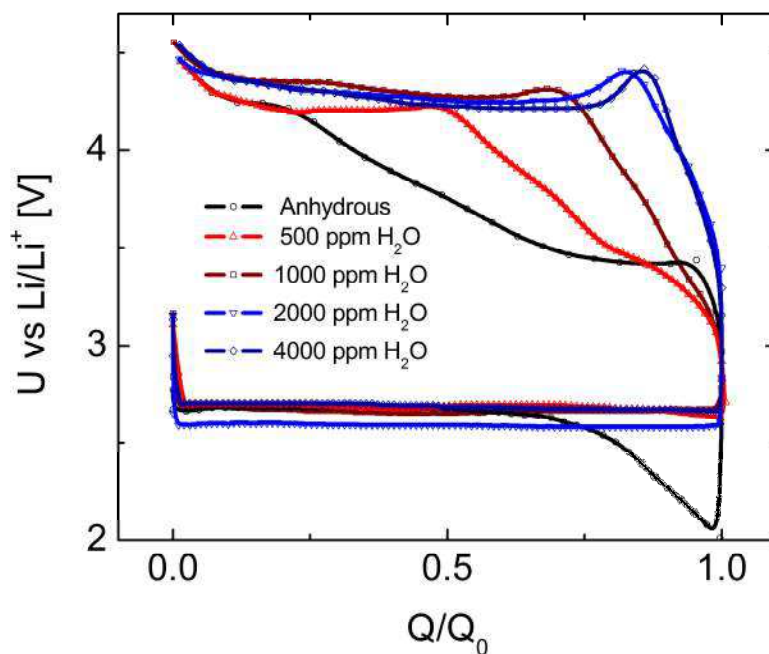


Figure S9| Charge potential variation with water content in the electrolyte. Discharge-charge curves for cells with XC72 cathodes that are discharged at a rate of 200 μA and employing 1M Li-TFSI in DME with varying water contents (shown in the legend) as the electrolyte. The x-axis is normalized to the full discharge capacity (Q_0) of the cathodes, which is 0.433 mAh for the cell employing a nominally anhydrous 1M Li-TFSI in DME as the electrolyte and 1 mAh for all the others. Clearly, the charge over potential increases rapidly to a value >4.2 V in the cells with water contaminated electrolytes. We believe that the charge over-potential is mainly due to the parasitic discharge products whose formation is accelerated in the presence of water as shown in Fig. S6 and S7.

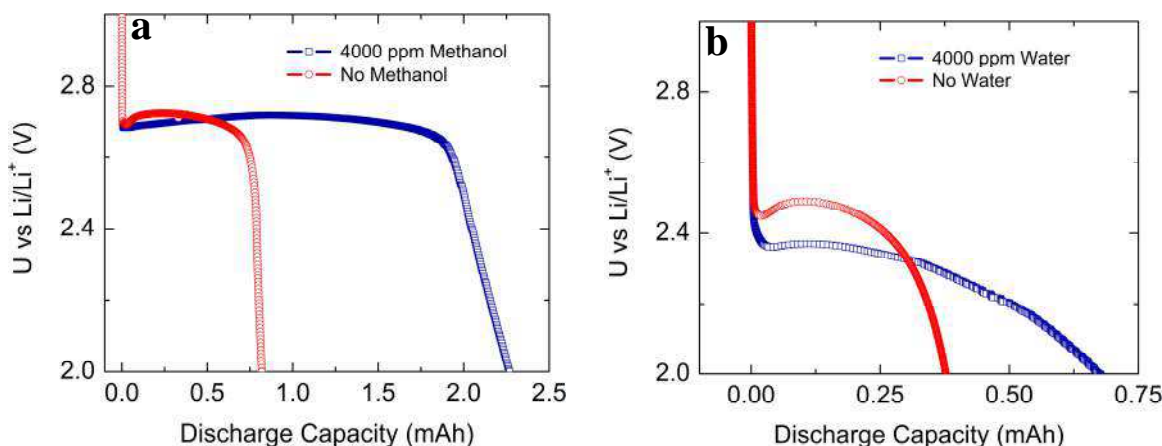


Figure S10| Discharge capacity comparison for methanol and water as additives in DME. **a**, Galvanostatic discharge curves at a discharge rate of 100 μA for cells employing 1M Li-TFSI in anhydrous DME and DME with 4000 ppm methanol as electrolytes. The total discharge capacity increases by 3 times in the presence of Methanol. In Fig. 6, we predicted that methanol, like water, has a high acceptor number and will therefore increase the solubility of O_2^- . This additional route to the formation of Li_2O_2 , we suggest, is the reason for enhanced capacity in the presence of methanol. **b**, Similar galvanostatic discharge curves at a discharge rate of 3 mA for cells employing 1M Li-TFSI in anhydrous DME and DME with 4000 ppm water as electrolytes. Even at this high discharge current of 3 mA, the increase in capacity due to water addition is close to 2 times the capacity obtained in the anhydrous case. Notably, with methanol as an additive and for water at high currents, we did not observe any Li_2O_2 toroid formation. Therefore, we suggest that the benefits of capacity enhancement by solution-mediated deposition of Li_2O_2 , are not restricted to low discharge rates.

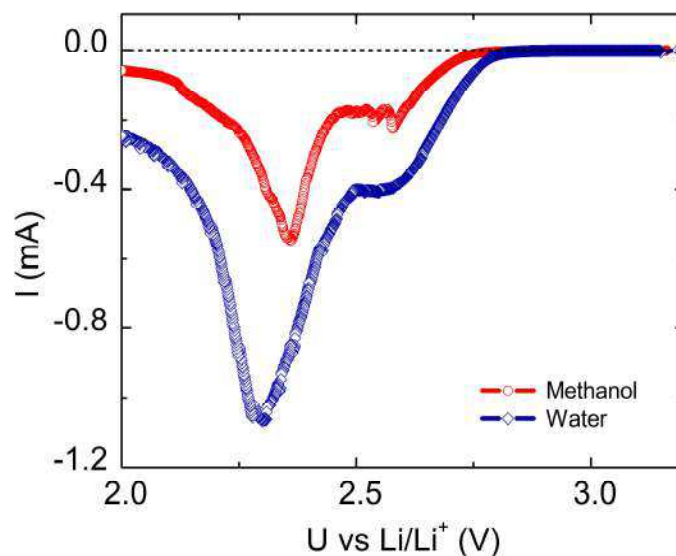


Figure S11| Linear scanning voltammograms with water and methanol. Discharge linear scanning voltammograms performed at 0.05 mV/s with a Vulcan XC72® carbon cathode and lithium anode employing 1M Li-TFSI based electrolyte solutions with 4000 ppm methanol (red) and 4000 ppm water (blue) as additives. The two LSV curves exhibit a distinct second peak at potentials <2.5 V, although with differing intensities. These LSV curves are consistent with our theoretical modeling based on the hypothesis that solvents with high acceptor number activate the solution-mediated growth of Li_2O_2 where O_2^- acts as a redox mediator.

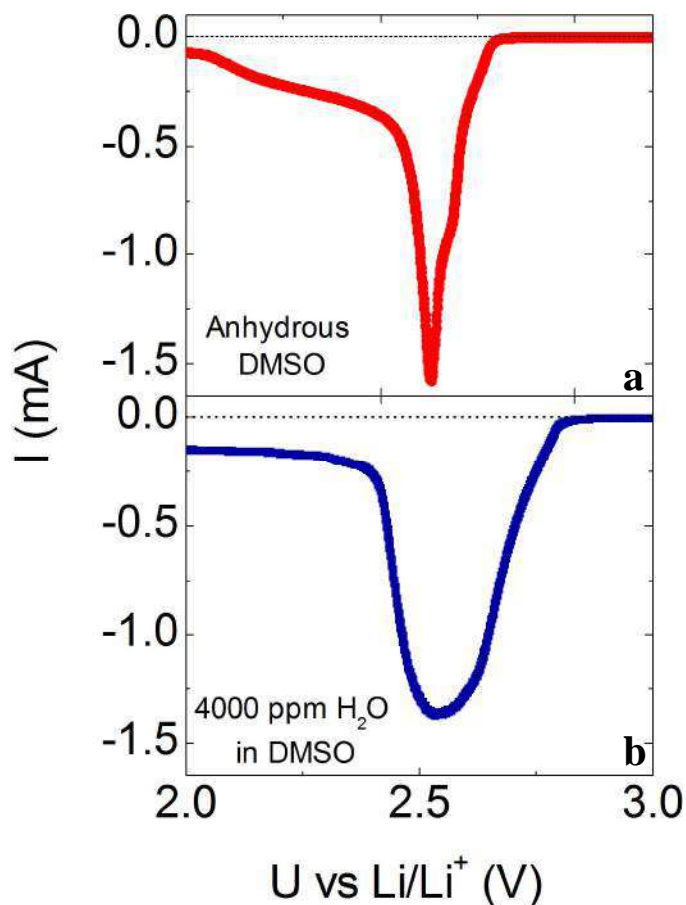


Figure S12| Discharge LSV curves for DMSO. The results of discharge LSV experiments performed at 0.05 mV/s with a Vulcan XC72® carbon cathode and lithium anode employing 1M Li-TFSI based electrolyte solutions in **a**, nominally anhydrous DMSO and **b**, DMSO with 4000 ppm water as the solvents. The anhydrous DMSO sample shows a sharp peak in the LSV at ~2.5 V with a very small, but distinct shoulder at ~2.3 V. As discussed in the main text, we attribute the peak at ~2.5 V to the surface electrochemical growth of Li_2O_2 and the one at ~2.3 V to the solution-mediated growth. The presence of this small shoulder correlates with the presence of toroids on the cathode (see Fig. S5a). By contrast, the LSV curve for the cell with 4000 ppm water exhibits a broad peak which is possibly due to the two above mentioned mechanisms of Li_2O_2 growth.

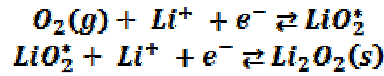
S3. Supplementary Text and Figures: Theory

Battery discharge model

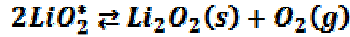
The model for simulating battery galvanostatic discharge is formulated as a set of differential algebraic equations (DAE). The galvanostatic condition is imposed as an algebraic equation defining the reaction rates and the material balances for the species associated with the electrochemical reactions are solved as coupled differential equations.

Surface electrochemical growth

The surface electrochemical growth of Li_2O_2 follows the sequential transfer of Li^+ and e^- as discussed in detail in our earlier work.³ The mechanism is given by:



Alternately, the second step could be,



This surface electrochemical growth could occur along different kind of sites such as kinks, steps and terraces. The overpotentials associated with the growth on these different sites have been calculated using density functional theory calculations in our earlier work⁷ and the same formalism is used to describe the surface electrochemical growth in our model. At the low current density conditions being simulated here, the surface growth of Li_2O_2 proceeds primarily along the kink and step sites of $\eta = 0.19$ V and $\eta = 0.28$ V respectively⁸ on the dominant (0001) surface (that is half O_2 converted at equilibrium). We assume the kinetic current density is described by the Tafel equation and is given by:

$$i_{\text{Li}_2\text{O}_2} = i_0 e^{-\max\left(\frac{(U-U_k)}{b_1}, 0\right)}$$

where,

$$U_k = U_0 - \eta = 2.85 - 0.19 = 2.66V \text{ and,}$$

$$U_s = U_0 - \eta = 2.85 - 0.28 = 2.57V$$

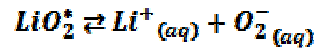
respectively, for the growth along the kink and step sites and b_1 refers to the Tafel slope, here chosen to be 120 mv per decade. When the potential, U is raised below U_i , the reaction becomes exergonic and loses its potential dependence and the current is given by the prefactor, i_0 . It must be noted that the ratios of kink and step sites need to be included to determine the overall rate and this is given by

$$i_{Li_2O_2,SURF} = \sum_k \theta_k i_{Li_2O_2,k}$$

where the index, $k \in \{\text{kink, step, terrace}\}$ and θ_k represents the surface coverage of site k ⁷. It is essential to note that the surface electrochemical growth includes the rate of electron transport through the discharge product, Li_2O_2 . In our earlier work, in the tunneling dominated regime, the rate of electron transport decays exponentially with the thickness of the discharge product⁸. The tunneling limit imposes that surface electrochemical growth shuts off at ~10 nm sized discharge products.

Solution growth

In this model, we consider a second possible route for the growth of Li_2O_2 . In water-contaminated cells (or a few other electrolytes/additives), we assume the generation of soluble reduced oxygen species. The mechanism for solution growth is initiated by the generation of soluble intermediate species in the presence of water, given by,



The free energy change associated with this dissolution process is given by,

$$\Delta G_{soln} = G_{LiO_2^*} - G_{Li^+} - G_{O_2^-} = G_{LiO_2^*} + [(G)_{Li} - G_{Li^+}] + [(G)_{O_2(g)} - G_{O_2^-}] - [(G)_{Li} + G_{O_2(g)})]$$

In different solvents, it has been shown that the redox potential shift of Li/Li^+ scales with the Gutman donor number of the solvent⁹

$$[(G)_{Li} - G_{Li^+}] \sim aDN$$

as given in Fig. S13. The stabilization of Li/Li⁺ saturates beyond a Gutman donor number of ~25 . For the redox potential shift of O₂/O₂⁻, a similar scaling is observed with the solvent's ability to accept electrons given by the Gutman acceptor number,

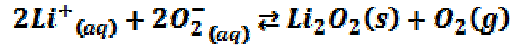
$$[(G]_{O_2(g)} - G_{O_2^-}) \sim bAN$$

(see fig. S14). Thus qualitatively, the free energy change associated with the activation of the solution process is given by

$$\Delta G_{soln} \sim aDN + bAN$$

where a ~ 0.1 and b ~ 0.01.

The solution soluble O₂⁻(aq) undergoes subsequent reaction on a growing Li₂O₂ particle leading to the formation of Li₂O₂ through the reaction given below:

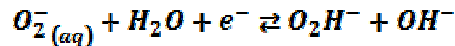


The solution route to the formation of Li₂O₂ essentially uses the soluble reduced oxygen as a redox shuttle to close the electrochemical cycle. Thus, the rate of electron transport through the discharge product does not directly affect the solution electrochemical growth rate as long as the Li₂O₂ formed by the surface electrochemical growth remains thin enough such that sufficient current to support the regeneration of O₂⁻ necessary for the solution electrochemical growth can be drawn through this insulating layer. The solution electrochemical growth depends on the water content as this determines the rate of soluble reduced oxygen species. The rate of solution electrochemical growth is then given by

$$i_{Li_2O_2,SOLN} = i_s c_{O_2^-}^2$$

where $c_{O_2^-}$ is the concentration of solution generated O₂⁻ and i_s is the prefactor which includes the diffusion rate of O₂⁻. i_s here is chosen to be 1 μA/cm².

In our model, we include an additional parasitic electrochemical reaction of the soluble reduced oxygen species with water leading to hydrogen peroxide, given by:



The current associated with this decomposition reaction is given by

$$i_{H_2O_2} = i_{0,H_2O_2} c_{O_2^-} c_{H_2O} e^{-\max\left(\frac{(U-U_{H_2O_2})}{b_1}, 0\right)}$$

where, $U_{H_2O_2}$ is the equilibrium potential for the formation of H_2O_2 . All Tafel slopes are assumed to be 120 mV/dec. Note that the formation of H_2O_2 is *not* associated with Li_2O_2 formation. It is simply a parasitic electrochemical/chemical reaction. $U_{H_2O_2}$ is assumed to be 2.6 V and $i_{0,H_2O_2} = 3 \text{ mA/cm}^2$.

The overall algebraic condition during discharge is given by

$$i = i_{Li_2O_2,SURF} + i_{Li_2O_2,SOLN} + i_{H_2O_2}$$

where i is the galvanostatic current of the cell.

In order to make quantitative comparisons of the results to the model to the experimental results, we also include some consumption of water at the lithium anode (as evidenced by some H_2 evolution during open circuit conditions with added H_2O). This consumption is assumed to be a chemical reaction obeying first order kinetics in the water concentration.

The algebraic condition imposes material balances for Li_2O_2 given by:

$$\frac{dV_{Li_2O_2}}{dt} = \frac{MW_{Li_2O_2} * i_{Li_2O_2}}{F \rho_{Li_2O_2}}$$

where $MW_{Li_2O_2} = 45.881 \frac{\text{g}}{\text{mol}}$ and $\rho_{Li_2O_2} = 2.31 \text{ g/cc}$ respectively. The other symbols have their usual meaning.

The concentrations of different species are given by the following differential equations:

$$\frac{dc_{O_2^-}}{dt} = k_1 c_{H_2O} - k_{-1} c_{O_2^-} - \frac{(2i_{Li_2O_2,SOLN} + i_{H_2O_2})}{F}$$

where $k_1 = 2 \times 10^{-5}$ and $k_{-1} = 10^{-5}$.

$$\frac{dc_{H_2O}}{dt} = -\frac{i_{H_2O_2}}{F} - k_{Li} c_{H_2O}$$

$$\frac{dc_{HO_2^-}}{dt} = \frac{i_{H_2O_2}}{F}$$

where $k_{Li} = 10^{-5}$.

Li₂O₂ Growth Model

The growth model describes the shape of the discharge product, incorporating surface and solution growth. The surface growth is homogenous and shuts down beyond the tunneling thickness. Thus, the surface growth produces a nearly uniform conformal growth on the surface.

Solution growth requires growth on existing Li₂O₂ site (likely a kink site on an already nucleated film). This relies on the fact that growth of Li₂O₂ on top of Li₂O₂ is easier than on C at low currents because of its lower overpotential. In our model, there are three processes that occur simultaneously.

- (i) There is a growth rate, r_{growth} associated with the solution process determined by the concentration of soluble reduced oxygen species and its diffusion as discussed above. The overall rate is ultimately set by the current density.
- (ii) A parasitic process that leads to the formation of an undesired insoluble product, such as LiOH or Li₂NH. This process leads to a surface layer that prevents further growth of Li₂O₂ determined by the parasitic rate, r_{par} .
- (iii) A vacancy defect generation rate, r_{def} on the parasitic film on Li₂O₂, which leads to the nucleation of a new layer when the surface is fully coated by the insoluble parasitic product.

In our model, we assume the defect generation rate is much smaller than the parasitic rate and the growth rate. Thus, this implies a time scale separation and this implies that this process can be simulated sequentially. Thus, the simulation is carried out in the following way.

- (i) Initially, a conformal film grows based on surface electrochemical route.
- (ii) Subsequently, we pick a defect nucleation site, at a given r , chosen by the appropriate probability distribution function (PDF) discussed below.
- (iii) We allow for the growth of Li₂O₂ discharge product both inward and outward from the nucleation site given by the growth rate, r_{growth} . At that same time, the

surface of the Li_2O_2 is being covered by the parasitic discharge product given by the rate, r_{par} .

- (iv) These two processes continue until a time t , when the entire surface is covered by the parasitic product. Growth can only proceed beyond this when another defect site is generated in the parasitic covering film. This is determined by the defect generation rate, r_{def} . Using our assumption, that the defect generation rate is much smaller than the growth and parasitic rates, the growth of each separate layer can be time separated and simulated separately. Thus, the simulation reverts back to step 2. This is repeated until the overall capacity (volume) obtained from the detailed electrochemical model is satisfied.

The discussions below use cylindrical symmetry to describe the different rates. We assume that the probability for growth is uniform over the entire surface and for a cylindrical disc, the probability of growth at given a surface element, dr , is given by $2\pi r dr$, where r is the radius of surface element from the center of some assumed growing particle. Thus, there is a greater likelihood of growth at the edges. Once, nucleated the particle can grow both inward and outward. After a time t , the total inward growth radius, r_{in} , and outward growth radius, r_{out} , is given by the material balance equation.

$$r_{\text{growth}} = \frac{MW_{\text{Li}_2\text{O}_2} * i_{\text{Li}_2\text{O}_2}}{F \rho_{\text{Li}_2\text{O}_2}}$$

$$V = r_{\text{growth}} t = \pi (r_{\text{n}}^2 - r_{\text{in}}^2) * d_{\text{layer}} + \pi (r_{\text{out}}^2 - r_{\text{n}}^2) * d_{\text{layer}}$$

where V is the total volume of the Li_2O_2 discharge product grown in time t past nucleation, r_{n} is the radial location of the nucleation point and d_{layer} is the thickness of the layer. Assuming equal likelihood to grow outward and inward, we get that $r_{\text{n}} - r_{\text{in}} > r_{\text{out}} - r_{\text{n}}$. This simply says that per unit of growth, outward growth generates greater surface area. This leads to expressions for both r_{in} and r_{out} as a function of time t .

At the same time, there is a parasitic chemical reaction rate due to the presence of the water. This leads to the covering of the Li_2O_2 surface and ultimately shutting off the Li_2O_2 growth process. This parasitic rate depends on the water concentration and is given by:

$$r_{par} = k_{par}c_{H_2O}$$

where k_{par} is the parasitic rate constant. The individual thickness of these layers, d_{layer} , is ultimately decided by the interplay between the growth rate and the parasitic rate. At low current rates and high H_2O concentrations, large diameter layers with a small d_{layer} are formed and the layers can then splay apart. However, at higher currents and/or smaller H_2O concentrations, the layers are smaller in diameter, i.e. the tendency to form toroids is suppressed (see Fig S18). This is observed in our simulations and consistent with the experimental results.

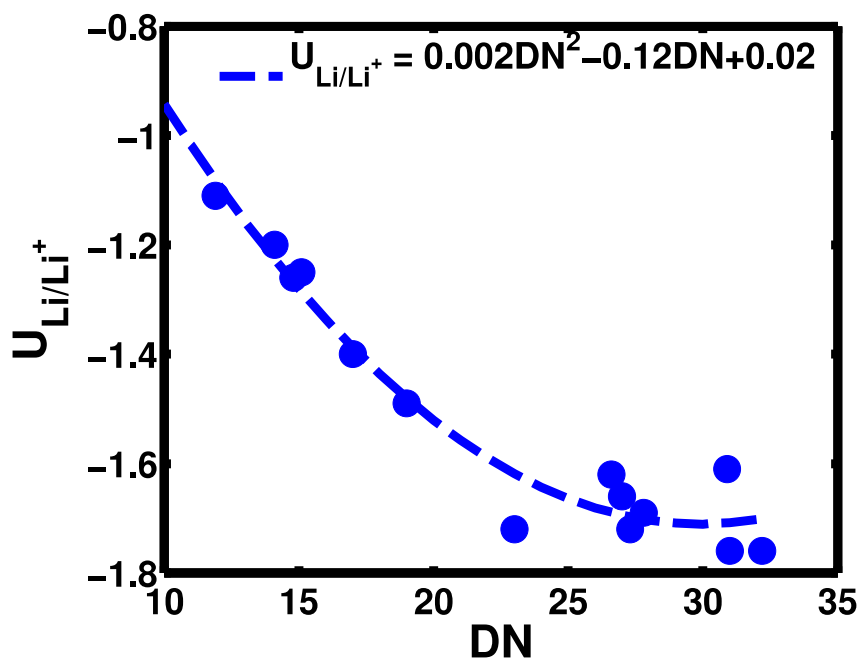


Figure S13| Li/Li⁺ redox potential versus Gutman donor number. A plot of the experimentally measured (filled blue circles) half-wave potentials of the Li/Li⁺ redox couple in different solvents plotted as a function of the Gutman donor number (DN). The experimental measurements are taken from the half-wave potentials measured by Gritzner *et al*¹⁰. The redox potential for the Li/Li⁺ redox couple is reported relative to Bis(biphenyl)chromium(I)/(0) couple. We observe a nearly linear dependence of the half-wave potential of Li/Li⁺ in the DN range 10-25. Beyond DN of 25, the theory predicts a saturation in the Li⁺ solvation leading to a nearly constant value of Li/Li⁺. A

best fit (quadratic) curve is shown in the plot and this quadratic relation is used in the generalization analysis for solution solubility presented in Fig 6.

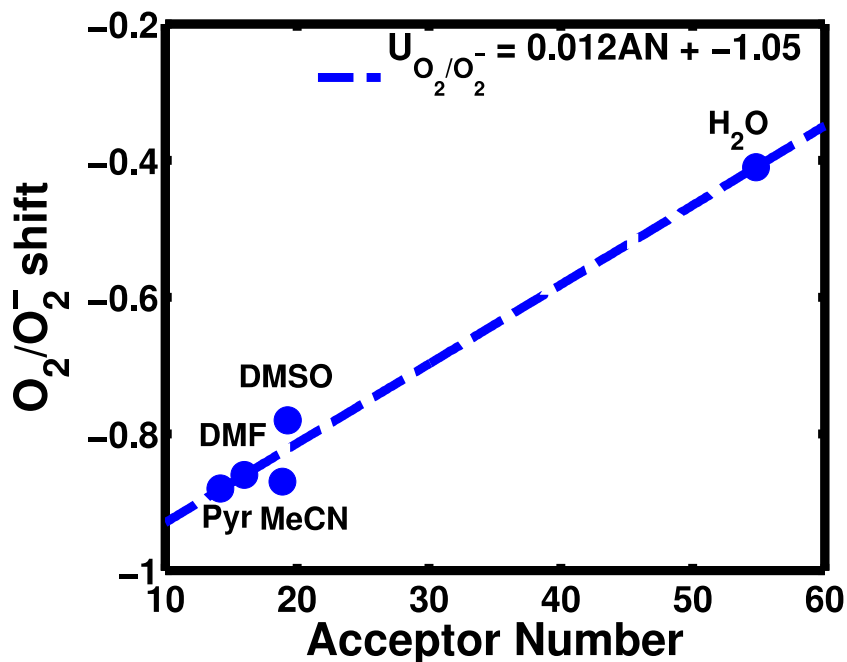


Figure S14| O_2/O_2^- redox potential versus Gutman acceptor number. A plot of the redox potential of O_2/O_2^- in different solvents as a function of Gutman Acceptor Number (AN). The experimental measurements for the redox potential have been taken from the work of Sawyer *et. al*¹⁰. The redox potentials of O_2/O_2^- is reported relative to Saturated Calomel Electrode (SCE). We observe a linear dependence of the redox potential with the Acceptor number. It is also to be noted that no trend is observed with DN as is to be expected. The best fit (linear) curve is shown in the plot and this linear relationship is used for the generalization of the solution mechanism discussed in the main text and presented in Fig 6.

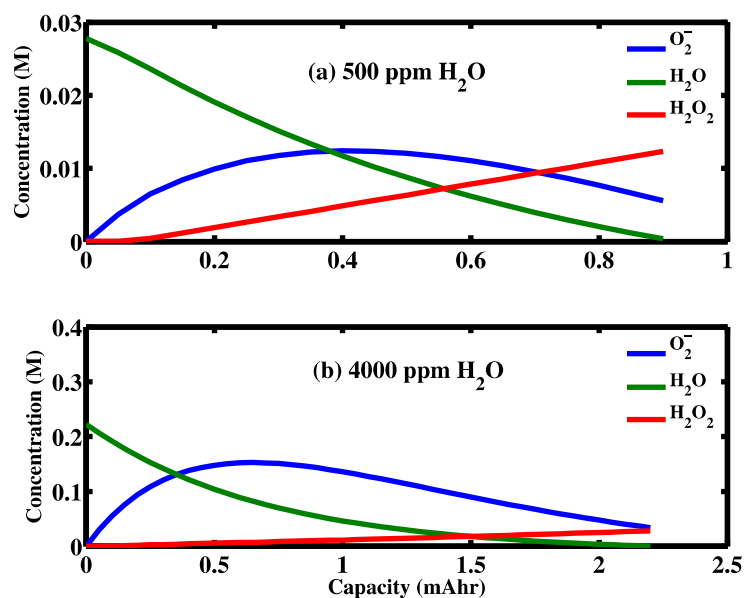


Figure S15| Concentration changes during discharge. Concentration profiles of O_2^- , H_2O and H_2O_2 as a function of capacity for **a**, 500 ppm and **b**, 4000 ppm water in the electrolyte which are obtained from the model under galvanostatic discharge at $I = 1 \mu A/cm^2$. In both cases, initially, there is a surge in the soluble O_2^- concentration. However, as time proceeds, water is being consumed through a parasitic reaction with the lithium metal and through superoxide anion's disproportionation¹¹ that we account for in the model. The latter leads to the formation of H_2O_2 , the time-dependent concentration of which is also plotted in the figure. The net decrease in water concentration leads to an overall decrease in the production rate of soluble O_2^- while the galvanostatic condition imposes a nearly constant consumption rate of O_2^- . Thus, we observe a net decay in the concentration of O_2^- , ultimately leading to cell death.

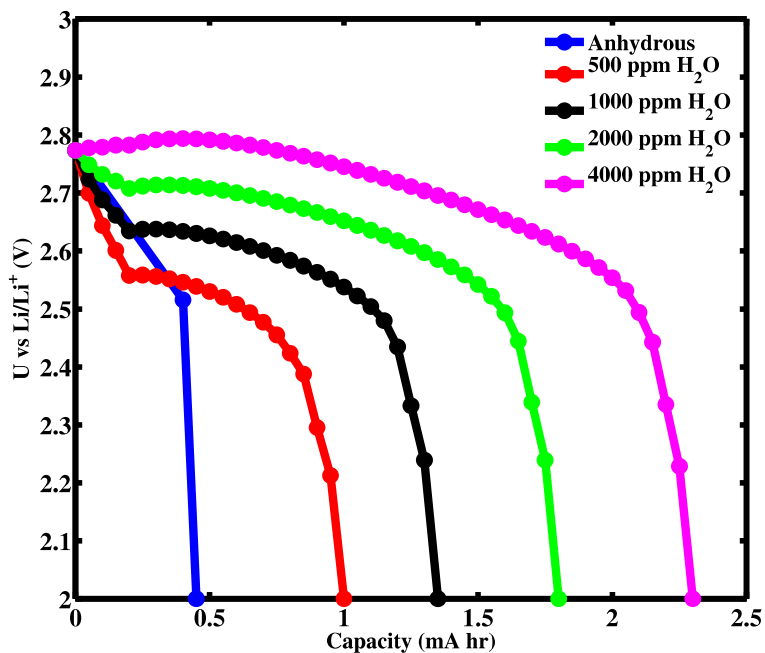


Figure S16| Theoretically predicted galvanostatic discharge curves. A plot of the cell potential (U vs Li/Li^+) as a function of capacity at three different water concentrations, anhydrous (blue), 500 ppm, 1000 ppm, 2000 ppm and 4000 ppm for a galvanostatic discharge rate of $I = 1 \mu\text{A}/\text{cm}^2$. We observe an increase in the capacity with increased water concentration due to an increased contribution through the solution pathway. There is a nearly ~ 5 fold enhancement in capacity at 4000 ppm of water relative to the anhydrous case. A normalization factor for surface area of $\sim 250 \text{ cm}^2$ is chosen such that the discharge capacity matches with that obtained from experiments.

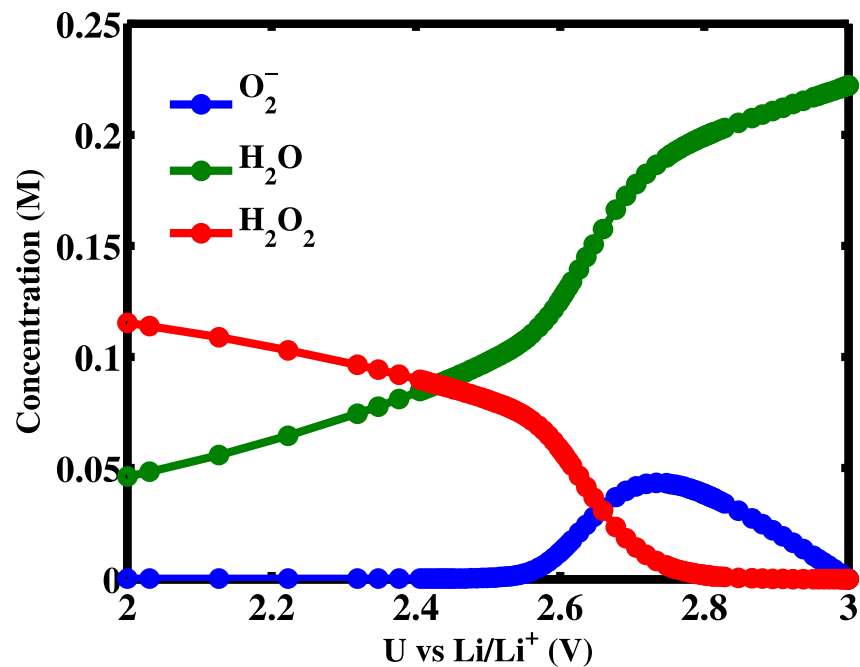


Figure S17| Theoretically predicted concentrations in a linear sweep voltammogram. Concentration profiles of O₂⁻, H₂O and H₂O₂ as a function of potential for 4000 ppm water in the electrolyte. As observed in the galvanostatic discharge, there is an increase in the soluble O₂⁻ concentration, which decays when the water is consumed into forming H₂O₂.

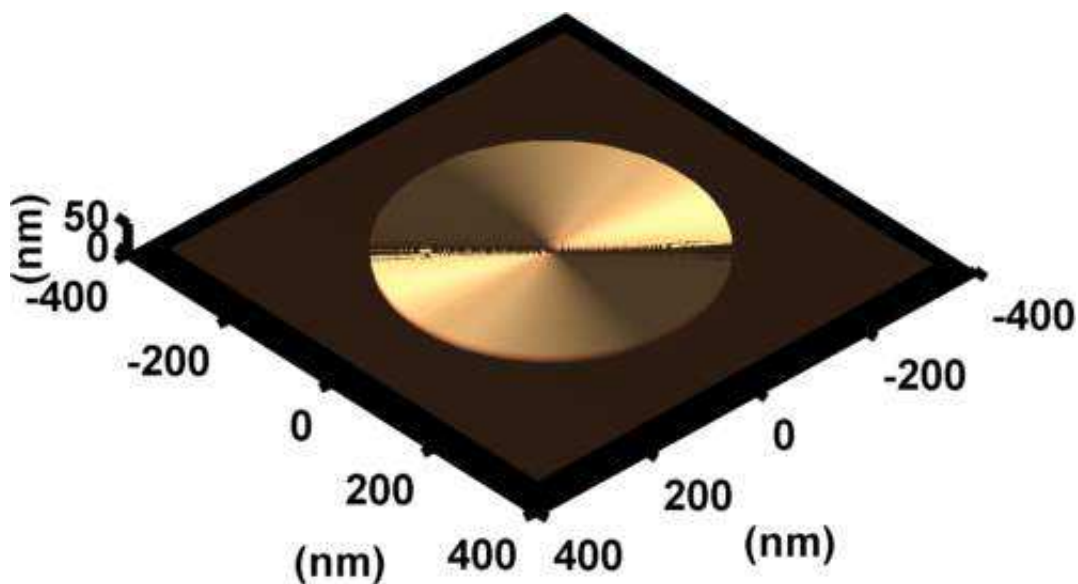


Figure S18| Particle morphology for the high current discharge, $i = 3 \text{ mA/cm}^2$ with 4000 ppm of H_2O . There is only a slight increase in the thickness of Li_2O_2 , with an almost conformal coating.

References

- 1 McCloskey, B. D., Bethune, D. S., Shelby, R. M., Girishkumar, G. & Luntz, A. C. Solvents' critical role in nonaqueous lithium–oxygen battery electrochemistry. *J. Phys. Chem. Lett.* **2**, 1161-1166 (2011).
- 2 McCloskey, B. D. *et al.* On the efficacy of electrocatalysis in nonaqueous Li–O₂ batteries. *J. Am. Chem. Soc.* **133**, 18038-18041 (2011).
- 3 McCloskey, B. D. *et al.* Combining accurate O₂ and Li₂O₂ assays to separate discharge and charge stability limitations in nonaqueous Li–O₂ batteries. *J. Phys. Chem. Lett.* **4**, 2989-2993 (2013).
- 4 Trucano, P. & Chen, R. Structure of graphite by neutron diffraction. *Nature* **258**, 136-137 (1975).

- 5 Cota, L. G. & de la Mora, P. On the structure of lithium peroxide, Li_2O_2 . *Acta Cryst. B* **61**, 133-136 (2005).
- 6 Lamb, J. *et al.* Mitigation of hydrogen capacity losses during pressure cycling of the $\text{Li}_3\text{N-H}$ system by the addition of nitrogen. *J. Phys. Chem. C* **115**, 14386-14391 (2011).
- 7 Hummelshoj, J. S., Luntz, A. C. & Norskov, J. K. Theoretical evidence for low kinetic overpotentials in Li-O_2 electrochemistry. *J. Chem. Phys.* **138**, 034703-034712 (2013).
- 8 Viswanathan, V. *et al.* Li-O_2 kinetic overpotentials: Tafel plots from experiment and first-principles theory. *J. Phys. Chem. Lett.* **4**, 556-560 (2013).
- 9 Viswanathan, V. *et al.* Electrical conductivity in Li_2O_2 and its role in determining capacity limitations in non-aqueous Li-O_2 batteries. *J. Chem. Phys.* **135**, 214704-214710 (2011).
- 10 Gritzner, G. Solvent effects on half-wave potentials. *J. Phys. Chem.* **90**, 5478-5485 (1986).
- 11 Sawyer, D. T., Chiericato, G., Angelis, C. T., Nanni, E. J. & Tsuchiya, T. Effects of media and electrode materials on the electrochemical reduction of dioxygen. *Anal. Chem.* **54**, 1720-1724 (1982).